A unicellular relative of animals generates an epithelium-like cell layer by actomyosin-dependent cellularization

Authors: Omaya Dudin*[1], Andrej Ondracka*[1], Xavier Grau-Bové[1,2], Arthur A. B. Haraldsen[3], Atsushi Toyoda[4], Hiroshi Suga[5], Jon Bråte[3], Iñaki Ruiz-Trillo[1,6,7]

* These authors contributed equally to this work.

Author Affiliations

[1] Institut de Biologia Evolutiva (CSIC-Universitat Pompeu Fabra), Passeig Marítim de la Barceloneta 37-49, 08003 Barcelona, Spain

[2] Department of Vector Biology, Liverpool School of Tropical Medicine, Pembroke Place, L3 5QA, Liverpool

[3] Section for Genetics and Evolutionary Biology (EVOGENE), Department of Biosciences, University of Oslo, Kristine Bonnevies Hus, Blindernveien 31, 0316 Oslo, Norway.

[4] Department of Genomics and Evolutionary Biology, National Institute of Genetics, Yata 1111, Mishima, Shizuoka 411-8540, Japan

[5] Faculty of Life and Environmental Sciences, Prefectural University of Hiroshima, Nanatsuka 5562, Shobara, Hiroshima 727-0023, Japan

[6] Departament de Genètica, Microbiologia i Estadística, Universitat de Barcelona, Avinguda Diagonal 643, 08028 Barcelona, Catalonia, Spain.

[7] ICREA, Passeig Lluís Companys 23, 08010 Barcelona, Catalonia, Spain.

Corresponding authors: omaya.dudin@outlook.com and andrej.ondracka@gmail.com

Summary

In animals, cellularization of a coenocyte is a specialized form of cytokinesis that results in the formation of a polarized epithelium during early embryonic development. It is characterized by coordinated assembly of an actomyosin network, which drives inward membrane invaginations. However, whether coordinated cellularization driven by membrane invagination exists outside animals is not known. To that end, we investigate cellularization in the ichthyosporean *Sphaeroforma arctica*, a close unicellular relative of animals. We show that the process of cellularization involves coordinated inward plasma membrane invaginations dependent on an actomyosin network, and reveal the temporal order of its assembly. This leads to the formation of a polarized layer of cells resembling an epithelium. We show that this epithelium-like stage is associated with tightly regulated transcriptional activation of genes involved in cell adhesion. Hereby we demonstrate the presence of a self-organized, clonally-generated, polarized layer of cells in a unicellular relative of animals.

Introduction

Cellularization of a coenocyte — a multinucleate cell that forms through sequential nuclear divisions without accompanying cytokinesis — is a specialized form of coordinated cytokinesis that results in cleavage into individual cells. Cellularization commonly occurs during development of animals and plants. In both, cellularization results in the formation of a multicellular, spatially organized epithelium-like structure. Despite the similarities, distinct mechanisms are involved in the cellularization of animal and plant coenocytes. During endosperm development in most flowering plants, coenocytes cellularize through cell wall formation around individual nuclei, forming a peripheral layer of cells surrounding a central vacuole (Hehenberger et al., 2012). This is coordinated by the radial microtubule system and is dependent on several microtubule-associated proteins (Pignocchi et al., 2009; Sorensen, 2002). In contrast, in a model animal coenocyte, the syncytial blastoderm of the fruit fly *Drosophila melanogaster*, cellularization is accomplished through plasma membrane invaginations around equally spaced, cortically positioned nuclei (Farrell and O'Farrell, 2014; Mazumdar and Mazumdar, 2002). This process is driven by a contractile actomyosin network (Mazumdar and Mazumdar, 2002). It depends on several actin nucleators, such as the Arp2/3 complex (Stevenson et al., 2002) and formins (Afshar et al., 2000). It also requires multiple actin-binding proteins, including myosin II (Royou et al., 2002), which mediates actin cross-linking and contractility, as well as septins (Adam et al., 2000; Cooper and Kiehart, 1996), cofilin (Gunsalus et al., 1995) and profilin (Giansanti et al., 1998). In addition, it depends on cell-cell adhesion proteins including cadherin, and alpha- and beta-catenin (Hunter and Wieschaus, 2000; Wang et al., 2004). This coordinated cellularization results in the formation of a single layer of polarized epithelial tissue, also known as cellular blastoderm (Mazumdar and Mazumdar, 2002). Such cellularization is common in insects, however, whether this mechanism of cellularization is found outside animals, remains unknown.

Among holozoans — a clade that includes animals and their closest unicellular relatives (Figure 1A) — ichthyosporeans are the only known lineage besides animals that forms coenocytes during their life cycles (Mendoza et al., 2002; de Mendoza et al., 2015). All characterized ichthyosporeans proliferate through rounds of nuclear divisions within a cell-walled coenocyte, followed by release of newborn cells (Marshall and Berbee, 2011, 2013; Suga and Ruiz-Trillo, 2013; Whisler, 1968). We have previously suggested that they undergo cellularization (Ondracka et al., 2018; Suga and Ruiz-Trillo, 2013). However, at present nothing is known about the ichthyosporean cellularization, and whether it involves animal-like mechanisms.

Here, we comprehensively characterized cellularization in the ichthyosporean *Sphaeroforma arctica,* in which we have previously shown that coenocytic cycles can be synchronized (Ondracka et al., 2018). We used imaging, transcriptional profiling, and pharmacological inhibition, to study the gene expression dynamics, morphological rearrangements, and mechanisms of cellularization. We found that cellularization is accomplished by inward plasma membrane invaginations driven by an actomyosin network, forming a polarized layer of epithelium-like cells. Time-resolved transcriptomics revealed sharply regulated expression of cell polarity and cell adhesion genes during this epithelium-like stage. Finally, we show that this process depends on actin nucleators and Myosin II, and we reveal the temporal order of the actomyosin network assembly. Together, these findings establish that cellularization of ichthyosporeans proceeds by an animal-like mechanism.

Results

Growth and cellularization in *S. arctica* are temporally separated stages of the coenocytic cycle

To determine the timing of cellularization in synchronized cultures, we established long-term live imaging conditions. Individual coenocytes exhibit growth in cell size until approximately 60 hours, after which they undergo release of newborn cells (Figure 1B, Movie S1). This was consistent with previous results in bulk cultures (Ondracka et al., 2018), confirming that our experimental setup for long-term live imaging faithfully reproduces culture growth. However, by measuring the diameter of the coenocytes, we observed that newborn cell release occurred with somewhat variable timing (Figure S1A, Movie S1).

Time-lapse imaging revealed that prior to cell release, the coenocytes darken along the periphery, and the dark front begins to advance towards the center (Movie S2). Afterwards, we observed an abrupt internal morphological change in the coenocyte, when the front disappears. We termed this event “flip” (Movie S2). The flip occurred in all the coenocytes and can be reliably detected on kymographs (Figure 1C). Aligning individual coenocyte size traces to this specific common temporal marker, we observe that coenocytes stop growing approximately 9 hours before the flip (Figure 1D and 1E). This shows that the growth stage and cellularization are temporally separated. The cellularization can be divided into a temporally less variable pre-flip phase (~9 hours) and a variable post-flip phase (Figure 1E and S1C). Taken together, these results show that growth and cellularization form temporally distinct stages of the coenocytic cycle of *S. arctica.* This provides a temporal framework in which to characterize phenotypically distinct stages of cellularization.

The cortical actin network establishes sites of membrane invagination and generates an epithelium-like layer of cells

To assess whether cellularization in *S. arctica* involves encapsulation of nuclei by plasma membranes, we imaged the plasma membrane using live time-lapse imaging in the presence of the lipid dye FM4-64 (Betz et al., 1996). We observed a rapid increase in FM4-64 intensity at the periphery of the coenocyte 30 minutes prior to flip (Figure 2A, panel II, Movie S3 and S4). The plasma membrane invagination sites formed at the periphery and progressed synchronously and rapidly from the outside toward the center of the coenocyte, forming polarized, polyhedral cells (Figure 2A, panels II-V, Movie S3 and S4). Finally, following flip, cells lost their polyhedral shape and became round, suggesting that they were no longer attached to each other (Figure 2A, panel VI, Movie S3 and S4).

In animal coenocytes, plasma membrane invagination is associated with dynamic organization of the actomyosin cytoskeleton (Mazumdar and Mazumdar, 2002). To investigate actin dynamics during cellularization, we took advantage of the timeline described above and imaged coenocytes that were fixed and stained for actin and nuclei (using phaloidin and DAPI, respectively) at different time points during cellularization (Figure 2B, S2A and S2B). During growth, actin localized exclusively as small patches at the surface of the coenocyte (Figure S2A, panel I). Only at the onset of cellularization, multiple actin patches increased in size to form actin nodes (Figure 2B, panel I and II, and S2A, panel II). This phase was followed by cortical compartmentalization surrounding the nuclei through gradual formation of an actin filament network solely at the cortex of the coenocyte (Figure 2B, panel III, and S2A, panels III and IV). Following this cortical compartmentalization, an epithelium-like cell layer was formed by inward growth of the actin filaments from the cortex to generate a structure resembling the cellular blastoderm in *Drosophila* (Figure 2B, panels IV and S2A, panels V and VI). During this stage, the actin signal intensity was uneven and higher on the internal side (Movie S5), and nuclei were localized close to the cortex, indicating that cells in this epithelium-like layer are polarized (Figure 2B, panel IV, Movie S5). The epithelium-like layer progressively grew towards the center of the coenocyte to fill the cavity, until the center space was occupied (Figure S2A, panel VII). After flip, similar to the plasma membrane organization mentioned above, the epithelium-like layer of cells was reorganized to form spherical cells (Figure 2B, panel VI, and S2A, panel VIII).

To determine the order of actin organization and plasma membrane invaginations, we assessed the localization of both actin and plasma membrane in fixed samples using phalloidin and a fixable analog of FM4-64 (FM4-64FX). We found that the cortical actin network formed prior to the appearance of the membrane dye (Figure 2C, panel II).

The intensity of FM4-64FX labeling also increased and co-localized with the underlying actin network around the time of plasma membrane invagination (Figure 2C, panels III and IV). This suggests that the cortical actin network determines the site of plasma membrane invagination.

Finally, to determine the timing of cell wall formation, we stained the cells with calcofluor. We observed that labeling co-localized with the membrane marker FM4-64FX around individual cells in the post-flip stage (Figure S2C). This shows that the newborn cells already build the cell wall before the release, as was suggested previously in other *Sphaeroforma* species (Marshall and Berbee, 2013).

In early insect embryos, cellularization of the syncytial blastoderm occurs through actin-dependent invagination of the plasma membrane. Here, we demonstrate that the cellularization of the ichthyosporean coenocyte also involves active actin reorganization and membrane invagination at the site of actin cytoskeleton. Additionally, this results in the formation of a polarized epithelium-like layer of cells with an internal cavity that morphologically resembles the cellular blastoderm of insects.

Cellularization is associated with extensive sequential transcriptional waves and is associated with evolutionarily younger transcripts

To gain insight into the regulation of the cellularization of *S. arctica*, we performed RNA-seq data on synchronized cultures with high temporal resolution, and comprehensively analyzed the dynamics of transcription, alternative splicing, and long intergenic non-coding RNAs (lincRNAs). Because the published genome assembly of *S. arctica* (Grau-Bové et al., 2017) was fragmented and likely resulted in incomplete gene models, we first re-sequenced the genome combining the Illumina technology with the PacBio long read sequencing technology. The final assembly sequences comprised 115,261,641 bp, and the metrics were greatly improved compared to the previous assembly (Grau-Bové et al., 2017) (Table S1). *Ab initio* gene annotation resulted in the discovery of novel ORFs due to the absence of repetitive regions in the previous assembly. RNA-seq data was used to improve the ORF prediction, to define the 5' and 3' untranslated regions, and to discover lincNAs. In total, 33,682 protein coding genes and 1,071 lincRNAs were predicted using this combined pipeline (see methods). This final transcriptome assembly was used as the reference transcriptome for further analysis.

To perform the time-resolved transcriptomics, we isolated and sequenced the mRNA from two independent synchronized cultures at 6-hour time intervals during the entire coenocytic cycle, encompassing time points from early 4-nuclei stage throughout growth and cellularization stages until the release of newborn cells (Figure S3A).

We first analyzed transcript abundance during the time series. The majority of the transcriptome (20,196 out of 34,753 predicted protein-coding and lincRNA genes) was transcribed at very low levels (mean expression throughout the time course <0.5 tpm [transcripts per million]) and were removed for the subsequent clustering analysis. Clustering of transcript abundance data from both biological replicates revealed a clear separation between the transcriptomes of the growth stage (12h to 42h time points) and the cellularization stage (48h to 66h time points) (Figure 3A). Furthermore, we observed that the transcriptome patterns between replicates 1 and 2 were shifted by 6 hours from 48 hours onwards (Figure 3A), presumably due to differences in temperature and conditions influencing the kinetics of the coenocytic cycle. We thus adjusted the time of the second replicate by 6 hours according to the clustering results, although we emphasize that the clustering analysis did not depend on time. Among the expressed transcripts (defined as mean expression levels higher than 0.5 tpm across all samples; in total 13,542 coding genes and 1,015 lincRNAs), consensus clustering using Clust (Abu-Jamous and Kelly, 2018) extracted 9 clusters of co-expressed transcripts with a total of 4,441 protein coding genes (Figure 3A), while the rest of the transcripts were not assigned to any co-expression cluster. The assigned cluster membership was robust to using either of the replicates or averaging (Figure S3B). Visualization by heatmap and t-SNE plot separated the clusters into two meta-clusters containing the growth stage (clusters 1-3, totaling 2,197 genes) and cellularization stage (clusters 4-9, totaling 2,314 genes) clusters (Figure 3C and 3D). Among the cellularization clusters, we see a clear temporal separation of different transcriptional waves, with clusters 5, 6 and 7 representing the three largest clusters of co-expressed transcripts of early, mid and late cellularization, respectively (Figure 3B and 3D). Altogether, this shows that cellularization is associated with extensive sharp transcriptional activation in multiple temporal waves, in total affecting 17% of the expressed transcriptome.

In parallel to transcript abundance dynamics, we also assessed alternative splicing (AS) across the time series. This analysis identified 2,022 genes affected by intron retention (12.9% of all intron-bearing genes, totaling 4,310 introns), 914 by exon skipping (12.3% of genes with >2 exons, 1,206 exons) and 44 with mutually exclusive exons (0.7% of genes with >3 exons, involving 118 exon pairs) in all samples (Figure S3C and S3D). Overall, neither the number of AS events nor the number of genes affected vary dramatically along the *S. arctica* growth cycle (Figure S3E-S3J). Analysis of AS events over time did not yield any discernible global dynamics, although we found a small number of events differentially present between the growth and cellularization stages (Figure S3K).

Interestingly, skipped exons were more likely to be in-frame (38.63%, compared to 30.33% of in-frame exons in genes with >2 exons, *p* = 4.34e-05, Fisher's exact test) and yield non-truncated transcripts, a phenomenon commonly observed in animal transcriptomes but not in transcriptomes of other unicellular eukaryotes (Grau-bové et al., 2018). The transcripts affected by such in-frame exon skipping events are enriched in biological processes such as regulation of multicellular organismal processes, assembly of the focal adhesion complex and cell growth (Figure S3L). Overall, although pervasive, alternative splicing likely does not play a major role in regulation of the coenocytic cycle and cellularization of *S. arctica*.

Additionally, we analyzed the dynamics of lincRNA expression. Overall, lincRNAs represent ~3% of total transcript abundance across the time series (Figure S4A). Among the long non-coding RNAs, 70 lincRNA transcripts clustered with coding genes into temporally co-expressed clusters (Figure 4A). Sequence homology search revealed that 24 of the *S. arctica* lncRNAs were conserved in distantly related ichthyosporean species such as *Creolimax fragrantissima*, *Pirum gemmata* and *Abeoforma whisleri* (estimated to have diverged ~500 million years ago (Parfrey et al., 2011). This is a remarkable depth of conservation, since animal lincRNAs are not conserved between animal phyla (Bråte et al., 2015; Gaiti et al., 2015; Hezroni et al., 2015). Other lincRNAs were either specific to *S. arctica* (511) or conserved only in closely related *Sphaeroforma* species (536). Comparison of lincRNA by degree of conservation showed no notable difference in %GC content (Figure S4B) or dynamics of expression during the coenocytic cycle (Figure S4C). However, we found that conserved lincRNAs were on average longer than non-conserved ones (Figure S4D) and, strikingly, expressed at much higher levels (Figure 4B). Among the 24 deeply conserved lincRNAs, 5 clustered in the temporally co-expressed clusters, which is higher than expected by chance (*p* = 0.0166, Fisher's exact test). Among these, 3 belonged to the cellularization clusters, including, lincRNA asmbl_31839, which has a remarkably high sequence similarity with its homologs from other ichthyosporeans (Figure S4E). Furthermore, its transcriptional regulation is independent of the transcriptional regulation of its neighboring coding genes (located within 3kb) (Figure 4C). In summary, we discovered deeply conserved lincRNAs that are expressed at high levels and are transcriptionally activated during cellularization.

Finally, to assess the evolutionary origins of the co-expression clusters, we used a phylostratigraphic analysis to classify genes into evolutionary gene age groups. We carried out orthology analysis of the predicted *S. arctica* proteome along with 30 representative species from the eukaryotic tree of life to identify "orthogroups" (i.e. groups of putative orthologs between species). *S. arctica* protein-coding genes clustered in 6,149 orthogroups representing 12,527 genes; the rest of the genes did not have an ortholog outside *S. arctica*.

Next, we inferred the age of each gene using Dollo parsimony (Csuros, 2010) to classify them into phylostrata (sets of genes with the same phylogenetic origin) (Figure 4D). Analysis of gene expression by phylostrata revealed a trend toward more variable expression throughout the coenocytic cycle in younger genes (Figure 4E), although their mean expression levels were lower (Figure S5A). Such a correlation has been observed in animal development, where developmentally regulated genes tend to be of younger origin (Domazet-Lošo and Tautz, 2010). Analysis of enrichment of gene phylostrata in each gene expression cluster (Figure S5B) showed that the growth clusters are enriched for pan-eukaryotic genes. In contrast, we find that the cellularization clusters were enriched for younger genes (Figure S5B and S5C). Importantly, we found that genes with ichthyosporean origins were significantly enriched in all three of the largest cellularization clusters (Figure S5B and S5C). Computing the transcriptome age index (Domazet-Lošo and Tautz, 2010) revealed an hourglass pattern, with older genes expressed at later stages of growth, and younger genes expressed during early growth and cellularization (Figure 4F). Such an hourglass transcriptomic pattern has previously been observed in animal development, where it reflects the morphological similarities and differences of embryos of different taxa (Domazet-Lošo and Tautz, 2010), and it has been suggested as a conserved logic of embryogenesis across kingdoms (Quint et al., 2012). Despite this, we currently do not have a morphological explanation for this transcriptional hourglass pattern in ichthyosporeans. Altogether, the phylostratigraphic analysis suggests that cellularization is a comparatively younger process, whereas the growth stage represent an evolutionarily ancient process.

Temporal co-expression of actin cytoskeleton, cell adhesion and cell polarity pathways during cellularization

To functionally assess the gene expression clusters, we also carried out gene ontology (GO) enrichment analysis (Table S2). The largest growth cluster (cluster 1) was enriched in GO terms related to cell growth and biosynthesis. Early and mid-cellularization clusters 5 and 6 were enriched for GO terms related to membrane organization and actin cytoskeleton. Late cellularization clusters were, in addition to GO terms related to actin, also enriched for GO terms related to cell adhesion and polarity. Given that these processes play a major role during cellularization of the insect blastoderm, we investigated the expression pattern of homologs of known regulators of cellularization in *Drosophila*.

In the *Drosophila* blastoderm, cellularization depends on the spatial organization of both the microtubule and actin cytoskeleton. It involves several microtubule and actin binding proteins, including kinesins, Myosin II, Myosin V, profilin (Chickadee), cofilin (Twinstar) and Septins, and the conserved family of Rho GTPases (Mazumdar and Mazumdar, 2002).

In *S. arctica,* we found that the expression of tubulins and kinesins, except for one (*S. arctica* Kinesin 2), is constant throughout the coenocytic cycle (Figure 5A and 5B). On the other hand, we found many actin-associated genes dynamically expressed. All actin nucleators of the formin family and members of the Arp2/3 complex peaked during cellularization (Figure 5C). In contrast to formins, which largely exhibited sharp peaks, the gene expression of the Arp2/3 complex was initiated earlier and increased gradually (Figure 5C). Septins, Cofilin, Profilin and Myosin V were temporally co-expressed during mid-cellularization and peaked at the same time as actin nucleators (Figure 5D), whereas myosin II, which has a role in organizing actin filaments and contractility, peaked later (Figure 5D). We likewise found the expression of all four members of the Cdc42/Rho1 orthogroup to be sharply activated during late cellularization (Figure 5E). Temporal co-expression of these genes suggests that the cellular pathways responsible for organizing the cytoskeleton and cell polarity in *Drosophila* cellularization are also involved in the cellularization process of *S. arctica*.

In addition to cytoskeletal organization, formation of a polarized epithelium also requires cell adhesion (Rodriguez-Boulan and Macara, 2014). Integrins and the cytoplasmic members of the integrin adhesome mediate cell-matrix adhesion in animal tissues. We observed that in *S. arctica*, both integrin receptors, alpha and beta, as well as all cytoplasmic members, are temporally co-expressed during late cellularization (Figure 5F). Beta and alpha catenin, together with cadherins in animals, mediate cell-cell adhesion in epithelial tissues (Rodriguez-Boulan and Macara, 2014). In *S. arctica*, we found three copies of Aardvark, a homolog of beta-catenin (Murray and Zaidel-Bar, 2014), as well as one homolog of alpha-catenin (Miller et al., 2013). We found that the expression of two out of three Aardvark transcripts, as well as the expression of the alpha catenin homolog, peaked during late cellularization (Figure 5F). This suggests that both cell-matrix and cell-cell adhesion pathways play a role in the establishment of the polarized epithelium-like structure during the late cellularization.

The actomyosin cytoskeleton is essential for cellularization

Finally, we tested whether disrupting the cytoskeleton would lead to defects in cellularization. In the absence of genetic tools, we used small inhibitory molecules that target specific conserved cytoskeletal components. We synchronized the cultures and added the inhibitors at the onset of cellularization (54 h time point). We first assessed the role of the microtubule cytoskeleton during cellularization by adding carbendazim (MBC), a microtubule depolymerizing agent (Castagnetti et al., 2007). Microtubule inhibition did not prevent plasma membrane invagination, although it resulted in a delay of flip and release of newborn cells (Figure 6A and 6B, and S6A, Movie S6 and Movie S7).

Furthermore, by staining the MBC-treated cells with DAPI and phalloidin, we observed a loss of the uniform spacing of the nuclei and actin filaments during the cortical compartmentalization stage of cellularization (Figure 6C). After MBC treatment, newborn cells varied in size and number of nuclei (Figure S6B, and S6C, Movie S6). These results suggest that the microtubule cytoskeleton is not essential for plasma membrane invagination but is crucial for nucleus and actin filament positioning at the cortex of the coenocyte.

Next, we sought to disrupt actin polymerization using either the broad actin depolymerizing agent Latrunculin A (LatA) (Braet et al., 1996), the Arp2/3 inhibitor CK666 (Hetrick et al., 2013), or the formin inhibitor SMIFH2 (Kim et al., 2015b). Cells treated with Latrunculin A lacked any actin patches or actin filaments and failed to undergo flip or produce newborn cells (Figure 6A-6C, Figure S6A, Movie S6 and S7). Furthermore, plasma membrane invagination did not occur after LatA treatment (Movie S6 and S7). In contrast, CK666-treated cells formed cortical actin patches, but were not able to form actin nodes, and they were unable to generate plasma membrane invaginations (Figure 6A-6C, Movie S6 and S7). These results show that the actin cytoskeleton and Arp2/3-mediated actin nucleation are required for the formation of actin nodes, the first step in the cellularization of *S. arctica*. In contrast, the formin inhibitor SMIFH2 did not block the formation of actin nodes, but it prevented the formation of actin filaments in the later stages (Figure 6A-6C). In addition, the plasma membrane invagination did not occur (Figure 6A-6C, Figure S6A, Movie S6 and S7), although we note that a small fraction of cells was not affected. This suggests that formins play a role in the nucleation of actin filaments after the formation of actin nodes.

Finally, we assessed the role of myosin II, using blebbistatin, an inhibitor of myosin II ATPase activity (Kovács et al., 2004). Blebbistatin treatment blocked plasma membrane invaginations and prevented cellularization (Figure 6A-6C, Figure S6A, Movie S6 and S7). Although blebbistatin-treated cells were able to form actin filaments, they had an aberrant wavy cortical actin filament network, suggesting that inhibition of myosin II causes loss of actin crosslinking and actin network contractility (Figure 6C). Taken together, these results indicate that the actomyosin apparatus is essential for cellularization in *S. arctica* and reveal a temporal sequence of involvement of Arp2/3 complex, formins and myosin II (Figure 6D). This temporal sequence is reflected in the relative timing of expression of Arp2/3, formins and myosin II genes (Figure 5C and 5D).

Discussion

To address whether animal-like cellularization leading to formation of an epithelium exists outside animals, we performed imaging, transcriptomic analysis and pharmacological inhibition in a unicellular relative of animals, the ichthyosporean *Sphaeroforma arctica* (Figure 6D). We show that at the onset of cellularization, Arp2/3 complex mediates the formation of actin nodes at the cortex of the coenocyte. This is followed by formin-dependent nucleation of actin filaments. These actin filaments are then crosslinked in a myosin II-dependent manner, which results in formation of a cortical actomyosin network that surrounds evenly-spaced nuclei. This spatial organization of both the actomyosin network and nuclei depends on microtubules. The localization of the actomyosin network determines the sites of plasma membrane invaginations and drives their inward growth, resulting in the formation of a polarized epithelium-like layer of cells. This stage co-occurs with transcriptional activation of genes involved in cell-cell and cell-matrix adhesion. Polarized growth of the epithelium-like layer persists until the internal cavity is fully occupied, after which the polarized polyhedrally-shaped cells undergo flip, lose polarization and detach from each other. At this point, future newborn cells form the cell wall before they are released and initiate a new coenocytic cycle. Overall, our results show that the cellularization of *S. arctica* morphologically resembles the cellularization of the *Drosophila* blastoderm, a model for animal coenocytes. Furthermore, the roles of Arp2/3, formins and myosin II, which are all essential for plasma membrane invagination during the cellularization in *Drosophila* blastoderm, are conserved between ichthyosporean and animal coenocytes.

Unlike in *Drosophila* early embryos, our transcriptomic analysis suggests that transcriptional control plays an important role in regulation of the coenocytic cycle of *S. arctica*. Interestingly, we show that many genes expressed during cellularization of *S. arctica* emerged at the onset of ichthyosporeans. This strongly suggests that the general mechanisms of cellularization in *S. arctica* are likely conserved within ichthyosporeans. Altogether, our results argue that cellularization in ichthyosporeans requires both pathways conserved in animals, as well as pathways exclusive to ichthyosporeans. The later may include lincRNAs that we found to be remarkably conserved among ichthyosporeans and show high expression levels. Overall, our temporal gene expression dataset provides a good resource for further functional studies in *S. arctica* and other ichthyosporean species.

The epithelium is the first tissue that is established during embryogenesis and perhaps the first that emerged in evolution, thus representing the basic form of multicellular organization in animals. Epithelia are characterized by apical-basal polarity and cell-cell junctions, mediated by cadherins and catenins, that segregates the internal medium from the outside environment (Rodriguez-Boulan and Macara, 2014).

Epithelia were found in all animal lineages, including sponges (Leys et al., 2009). It has previously been suggested that the origin of epithelial structures predates the origin of animals, as a polarized epithelium-like structures, regulated by alpha- and beta-catenins, is also present in the slime mold *Dictyostelium discoideum* (Dickinson et al., 2011). Based on this finding, it has been suggested that all unikonts (Amorphea) — a clade including animals, its close holozoan unicellular relatives, as well as Fungi, Apusomonadida, Breviatea, and Amoebozoa — evolved from an ancestor with simple multicellular organization (Dickinson et al., 2012). However, epithelial structures have not yet been observed in other unikont lineages besides animals and slime molds (Brunet and King, 2017), raising questions whether the origin of these epithelial structures in these two relatively divergent lineages might have originated independently.

Here we argue that epithelium-like structures are generated during cellularization of ichthyosporeans. We show that the epithelium-like layer of cells is polarized due to the asymmetrical localization of cellular components and the direction of growth. Furthermore, despite lacking genetic tools to demonstrate the function of alpha and beta catenin, the sharp expression of catenins during the epithelium-like stage of cellularization strongly suggests a function in cell-cell junctions. However, whether this layer of cells functions to segregate the interior of the coenocyte from the outside environment remains to be addressed. Our results in ichthyosporeans lends support to the hypothesis that the origin of epithelial tissues predates the origin of animals. However, unlike the epithelium formation in social amoebae, which originates through aggregation (Bonner, 1998), ichthyosporean epithelium is generated clonally, such as epithelial tissues in all modern animals. Further studies to better understand the mechanisms of epithelium formation in ichthyosporeans will provide insight into the evolutionary origin of one of the defining features of animal multicellularity, the spatiotemporal cellular organization of tissues.

Author contributions

O.D. and A.O. designed the study and set up the methodology. O.D. performed the microscopy and chemical inhibition experiments. A.O. performed the *S. arctica* RNA extraction, flow cytometry, and analyzed the gene expression data. A.T. and H.S. sequenced and assembled the *S. arctica* genome. X.G.-B. performed the genome annotation and alternative splicing analysis. A.A.B.H. and J.B. performed the de-novo transcriptome annotation, lincRNA prediction and conservation analysis. I.R.-T. provided supervision. O.D., A.O. and I.R.-T. wrote the original draft. All authors reviewed and edited the manuscript.

Acknowledgments

We thank Sophie Martin, Aaron New, Daniel Richter and Sébastien Wielgoss for discussion and comments on the manuscript, Takaaki Kai for discussion on the ichthyosporean development, Eduard Ocaña for advice on the phylostratigraphic analysis, and Meritxell Antó for technical support. We also acknowledge the UPF Flow Cytometry Core Facility for assistance with flow cytometry, CRG Advanced light microscopy unit for support with confocal imaging, and the CRG Genomics Unit for mRNA library preparation and Illumina sequencing. This work is dedicated to the memory of Arthur Haraldsen, our dear friend and colleague, who tragically passed away during the final stages of the manuscript preparation.

This work was funded by European Research Council Consolidator Grant (ERC-2012-Co -616960) to I.R.-T.; MEXT KAKENHI (grant Nos. 221S0002 to A.T.; grants no 26891021 and 16K07468 to H.S.); and a Young Research Talents grant from the Research Council of Norway (grant no. 240284) to J.B.. O.D. was supported by a Swiss National Science Foundation Early PostDoc Mobility fellowship (P2LAP3_171815) and a Marie Sklodowska-Curie individual fellowship (MSCA-IF 746044). A.O. was supported by a Marie Sklodowska-Curie individual fellowship (MSCA-IF 747086).

Declaration of interests

The authors declare no competing interests.

Methods

Culture conditions

Sphaeroforma arctica cultures were grown and synchronized as described previously (Ondracka et al., 2018). Briefly, cultures were grown in Marine Broth (Difco BD, NJ, USA; 37.4g/L) in flasks at 12ºC until saturation, producing small cells. These cells were then diluted into fresh media with low density (1:300 dilution of the saturated culture), resulting in a synchronously growing culture. Cultures of *S. gastrica*, *S. tapetis*, *S. nootkatensis*, *P. gemmata* and *A. whisleri* were similarly kept in Marine Broth (Difco BD, NJ, USA; 37.4g/L) at 12°C in dark conditions.

Sphaeroforma arctica genome sequencing and assembly

Genomic DNA from *S. arctica* was extracted using QIAamp DNA Blood Midi Kit (Qiagen) from 300 mL culture incubated at 12 C° for 1 week in six 75 cm^2 flasks. The Qubit (Invitrogen) quantification found ~150 µg genomic DNA in total.

A SMRTbell library for P6/C4 chemistry was constructed and was run on 32 SMRT cells in a PacBio RSII system (Pacific Biosciences), generating 2,209,004 subreads with a total of 25,164,714,269 bp. Raw subreads were first assembled using the FALCON_unzip assembler (v0.4.0) and the initial assembled sequences were polished by the Quiver integrated in SMRT analysis (v2.3.0). Genomic DNA was then sheared using a Focused-ultrasonicator (Covaris, Inc.). A paired-end library with an insert size of 600 bp was sequenced on an Illumina HiSeq2500 platform, producing 136,566,600 reads with read length of 250 bp. Paired-end reads were mapped against the polished sequences using the BWA mem (v0.7.12) followed by error-correction using Pilon (v1.22) (Walker et al., 2014).

Sphaeroforma arctica gene annotation

We annotated predicted gene models in our scaffolds using BRAKER2 (Hoff et al., 2018). First we used STAR 2.7 (Dobin et al., 2012) to map all the RNA-seq samples to the genomic scaffolds, so as to obtain empirical evidence of gene bodies and guide the prediction of gene coordinates. These read mappings were then supplied to BRAKER2 in BAM format, which combied these external evidence with the gene coordinates predicted by Augustus 3.2.2 (Keller et al., 2011) (--noInFrameStop mode) and Genemark v4.21 (Lomsadze et al., 2005) to obtain a consolidated set of gene models in GFF format.

The transcriptome of *S. arctica* was assembled in order to add 5' and 3' UTR regions to the genome annotation and to search for long non-coding RNA-seq using data obtained here (see below).

The RNA-seq reads from the first time series replicate (excluding timepoint 30) were subjected to quality trimming and adaptor removal using Trimgalore (v0.4.5) (http://www.bioinformatics.babraham.ac.uk/projects/trim_galore/) and Trimmomatic v0.35 (Bolger et al., 2014). Trimgalore was first run to remove sequencing adaptors, allowing 0 mismatch and minimum adaptor length of 1 nt. Trimmomatic was run by trimming bases with phred score <20 from both ends. Furthermore, a sliding window of 4 bases was used to trim reads from the 5' end when the mean phred score dropped below 20. Finally, the IlluminaClip option was used to search for remaining sequencing adaptors, allowing 2 seed mismatches, a palindrome clip threshold of 20 and minimum single match threshold of 7 nt. The quality filtered RNA reads were subsequently assembled using Trinity v2.5.1 (Grabherr et al., 2011), running both a *de novo* and a genome-guided assembly. To perform a genome-guided transcriptome assembly, we first mapped the RNA-seq reads against the genome using Hisat2 v2.1.0 (Kim et al., 2015a), in strand-specific mode with default parameters. Both Trinity assemblies were run in strand-specific mode while applying the jaccard clip option and otherwise default parameters. We next evaluated the strand-specificity of the assemblies by mapping RNA-seq reads back to the Trinity assemblies using scripts supplied within the Trinity software. Transcripts were subsequently removed if >80% of the reads mapped in the wrong direction. The PASA pipeline v2.3.1 (Haas et al., 2003) was then used to update the existing genome annotation. First, the assembled transcripts described above were mapped against the genome using the initial PASA script to make a temporary annotation file. This was performed with default parameters, using both Blat v35 (Kent, 2002) and Gmap v2015-09-29 (Wu and Watanabe, 2005) aligners, with transcripts specified as strand-specific. Lastly, the transcriptome-based annotations were compared with the existing genome annotation in a final PASA run, also using default parameters. In this step, the existing genes were expanded with UTR annotations and, in cases where a single RNA transcript covered multiple genes, these become merged into a single gene.

RNA isolation, library preparation and sequencing

Synchronized cultures of *Sphaeroforma arctica* at 12ºC were sampled every 6 hours for a total duration of 72 hours. Total RNA was extracted by Trizol and purified using the miRNeasy Mini Kit (QIAGEN) from ~50mL of culture at each time point. Libraries were prepared using the TruSeq Stranded mRNA Sample Prep kit. Paired-end 50bp read length sequencing was carried out at the CRG genomics core unit on an Illumina HiSeq v4 sequencer. We obtained between 19 and 32 M reads per sample. Transcripts were quantified using Kallisto software (Bray et al., 2016) with default parameters. To remove non-expressed genes, we filtered out transcripts that had a mean expression level of <0.5 tpm across all 20 samples. This resulted in a set of 14557 transcripts that were used for clustering.

For *S. gastrica* and *S. tapetis*, RNA purification was performed using the RNeasy kit (Qiagen), while for *S. nootkatensis*, *P. gemmata* and *A. whisleri*, RNA was purified using Trizol (Invitrogen, CA, USA). Strand-specific sequencing libraries were prepared using Illumina TrueSeq Stranded mRNA Sample Prep kit and sequenced on an Illumina HiSeq3000 machine (150 bp paired end).

Clustering of the gene expression and gene ontology enrichment analysis in *S. arctica*

Sphaeroforma arctica transcripts were clustered by their gene expression profiles using Clust software (Abu-Jamous and Kelly, 2018) with default parameters and automatic normalization mode. This yielded 4511 transcripts (4441 coding genes and 70 lncRNA genes) that were clustered into 9 clusters, ranging from 41 to 2081 co-expressed genes. Gene expression profiles were visualized using superheat package in R (Barter and Yu, 2018). The tSNE plot was generated using Rtsne package.

Gene Ontology enrichments based on the GOs annotated with eggNOG mapper (Huerta-Cepas et al., 2017) were computed using the topGO R library (v. 2.34). Specifically, we computed the functional enrichments based on the counts of genes belonging to the group of interest relative to all annotated genes, using Fisher's exact test and the elim algorithm for ontology weighting (Alexa et al., 2006).

Transcriptome assembly of other unicellular holozoans

Raw reads (from sequencing libraries and SRA data) were processed with Trimmomatic (Bolger et al., 2014) to remove adapters and low-quality bases, by trimming bases with phred score <28 from both ends. Furthermore, a sliding window of 4 bases was used to trim reads from the 5' end when the mean phred score dropped below 28. Finally, the IlluminaClip option was used to search for remaining sequencing adaptors, allowing 2 seed mismatches, a palindrome clip threshold of 28 and minimum single match threshold of 10 nt. All libraries were assembled denovo with Trinity (v2.3.2– 2.5.1) (Grabherr et al., 2011) using default parameters. The assemblies of RNA-seq data were performed with the strand specific option, while assemblies based on SRA data were run in standard mode. For the *S. sirkka* assembly we also applied the jaccard clip option. Coding regions were predicted using TransDecoder v5.2.0 (Haas et al., 2013), by first extracting the longest possible ORFs (only top strand was searched in the strand-specific assemblies), on which likely coding region was predicted. Only the longest ORF was kept for each transcript.

DNA isolation and genome assembly of *S. gastrica* and *S. tapetis*

Genomic DNA (gDNA) was isolated from *S. gastrica* and *S. tapetis*, by lysing cells on a FastPrep system (MP Biomedicals, CA, USA; 4m/s, 20s) followed by gDNA purification using the DNeasy kit (Qiagen, NRW, Germany) and subsequently sequenced on an Illumina HiSeq X system (150 bp paired end). Raw reads were subjected to quality trimming and adaptor removal as described above for RNA-seq data, with a phred score cut-off of 26.

The quality trimmed reads were subsequently error-corrected and assembled using Spades v3.10.0 (Nurk et al., 2013) applying kmer values 21, 33, 55, 77, 99 and 121, but otherwise default parameters. The resulting spades assemblies were scaffolded using L_rna_scaffolder (Xue et al., 2013) and polished with Pilon (Walker et al., 2014). L_RNA_Scaffolder was run by first mapping the respective transcriptome assemblies to the genome assemblies using Blat (Kent, 2002) which was inputted to L_rna_scaffolder. Next, we run Pilon by first mapping the quality trimmed genomic Illumina reads to the genome assembly using Bowtie2 (Langmead et al 2012). The resulting mapping file was then used in Pilon with default parameters. L_rna_scaffolder and Pilon were run repeatedly 5 times, followed by 3 final runs using only Pilon. These genome assemblies were used as reference genomes for genome-guided Trinity assemblies and PASA annotation as previously described for *S. arctica*.

S. arctica long intergenic non-coding RNA identification and conservation analysis

Long intergenic non-coding RNAs (lincRNAs) were identified from the PASA annotation described above. First, transcripts shorter than 200 nt were discarded. Then, coding potential was evaluated using both TransDecoder (Haas et al., 2013) and CPC2 (Kang et al., 2017) with default parameters. All transcripts lacking coding potential were then compared with the Rfam database (Kalvari et al., 2017) to exclude other non-coding RNAs such as rRNAs and tRNAs. To exclude possible UTRs actually belonging to fragmented protein coding genes, a minimum genomic distance of 1000 bp from the closest protein coding gene was required. The remaining transcripts were compared with protein coding genes in the Swissprot database using Blastx (Altschul et al., 1990), and all sequences with a match better than e-value 1e-5 were removed.

Next, the potential lncRNA transcripts were blasted against the proteomes of *S. arctica* and other closely related ichthyosporeans (*Sphaeroforma tapetis*, *Sphaeroforma sirkka*, *Sphaeroforma nootkatensis*, *Sphaeroforma napiecek*, *Sphaeroforma gastrica*, *Creolimax fragrantissima*, *Pirum gemmata* and *Abeoforma whisleri*), and all transcripts with a match better than e-value 1e-5, were discarded. To remove transcripts resulting from potential spurious transcription, we required a minimum expression level of at least 1 tpm in at least one time series sample.

To search for possible conserved lncRNAs in other species, we performed Blastn searches against transcriptomes and genomes of several holozoan species (Richter et al., 2018) (Table S3). All genes providing hits with an e-value less than 1e-50 were considered to be a conserved homolog.

Genome-wide analysis of alternative splicing

Each RNA-seq run was independently aligned to the *Sphaeroforma* genome using Hisat2 (Kim et al., 2015a), using default parameters except for longer anchor lengths to faciliate *de novo* transcriptome assembly (--dta flag).

The resulting alignments (in SAM format) were used to build sample-specific transcriptome assemblies with Stringtie2, using existing gene models (in GFF format, -G flag) as a reference, a minimum isoform abundance of 0.01 (-f flag) and a minimum isoform length of 50 bp (-m flag). For each sample, we only retained transcripts that overlapped with known genes in the final GFF file (using bedtools (Quinlan and Hall, 2010)). Then, we built a consolidated set of isoforms by pooling all sample-specific GFF annotations and the reference annotation using Stringtie2 (--merge flag), without imposing any limitation of minimum expression levels (-T flag set to 0), and retaining isoforms with retained introns (-i flag). We also calculated the expression levels at the isoform level using Salmon (Patro et al., 2017) (output in TPM). Then, we used SUPPPA2 (Trincado et al., 2018) to generate a set of alternative splicing events, for which their frequencies were calculated for each sample. Specifically, we used the consolidated set of isoforms (GFF format) to obtain a list of all possible AS events using SUPPA2 *generateEvents* mode (setting the output to exon skipping [SE], mutually exclusive exons [MX] and intron retention [RI]), and -l 10. Then, we used SUPPA psiPerEvent mode to calculate the PSI values of each AS event for each sample, using the expression levels of each isoform (obtained from Salmon) as a reference. Differential splicing was quantified by calculating the calculating the differential PSI values between the average of each sample group (growth stage [t=12h to t=48h] compared to cellularization stage [t=54h to t=66h]). *p*-values were obtained using the empirical significance calculation protocol described in SUPPA2.

After running SUPPA2, we produced functional annotations of the effect of each AS event on the final transcript. First, we annotated the protein domains in our consesus gene models using Pfam (version 31) and Pfamscan. These protein-level coordinates were converted to genomic coordinates using BLAT alignments (version 36, by aligning protein sequences to 6-frame translations of the genome) (Kent, 2002) and intersected with the genomic coordinates of AS events using the GenomicRanges and IRanges libraries (*findOverlapPairs* module) (Lawrence et al., 2013) from the R statistical framework (version 3.5.2). Second, we used the genomic coordinates of all AS events to recode each AS event as insertion/deletion variants that were amendable for analysis using the Variant Effect Predictor software (version 92.3) (McLaren et al., 2016) (SE were encoded as deletions, RI as insertions, and MX as insertion/deletion complex events). VEP produced a list of the effects of each AS variant (according to the Sequence Ontology nomenclature (Eilbeck et al., 2005)), using our consensus gene models as a reference.

Phylostratigraphy analysis

First, we performed gene orthology assignment by searching for orthologs in a representative set of 30 publicly available eukaryotic proteome sequences (animals: *H. sapiens, S. kowalewskii, D. melanogaster, T. tribolium, N. vectensis, T. adherens, M. leidii and A. queenslandica*; choanoflagellates: *S. rosetta*; filastereans: *C. owczarczaki* and *M. vibrans*; teretosporeans: *S. arctica, C. fragrantissima, I. Hoferi, A. whisleri, C. perkinsii, P. gemmata, S. destruens, C. limatocisporum,* fungi: *F. alba, C. anguillulae, S. punctatus, M. verticillata* and *S. pombe*; other eukaryotes: *T. trahens, A. castellanii, D. discoideum, N. gruberi, T. thermophila, E. huxleyi, A. thaliana* and *P. yezoensis*) using orthofinder (Emms and Kelly, 2015) in Diamond mode. The generated orthogroups were used to determine orthologs of *S. arctica* genes in other species, unless a phylogeny of a specific gene family has been published. We then determine gene age of each orthogroup by Dollo parsimony implemented in Count software (Csuros, 2010) to classify the *S. arctica* proteome into 10 phylostrata, ranging from paneukaryotic to *S. arctica*-specific. The transcriptome age index was computed using a formula defined in (Domazet-Lošo and Tautz, 2010).

Flow cytometry

Flow cytometry was performed as described previously (Ondracka et al., 2018) Cells were fixed in 4% formaldehyde, 1M sorbitol solution for 15 minutes at room temperature, washed once with marine PBS (PBS with 35 g/L NaCl), and stained with DAPI (final concentration 0.5 μg/mL) in marine PBS. Samples were analyzed using an LSRII flow cytometer (BD Biosciences, USA) and the data were collected with FACSDiva software. DAPI signal was measured using a 355nm laser with the 505nm longpass and 530/30nm bandpass filters. Approximately 2,000 events were recorded in each measurement. The flow cytometry data were processed and analyzed using FloJo software (Ashland, OR).

Microscopy

Confocal microscopy of the spatiotemporal organization of actin in Figure 2A and Movie S5, was performed using a confocal laser scanning Leica TCS SP5 II microscope with an HC PL APO 63x/1.40 Oil CS2 oil objective. All remaining live and fixed images were obtained using a Zeiss Axio Observer Z.1 Epifluorescence inverted microscope equipped with Colibri LED illumination system and an Axiocam 503 mono camera. A Plan-Apochromat 63X/1.4 oil objective has been used for imaging fixed cells (Figures 2C, S2A, 6B, 6C), and an EC Plan-Neofluar 40x/0.75 air objective for supplementary Figure 2C, Movies S3 and S4 and an N-ACHROPLAN 20x/0.45na Ph2 air objective for live imaging in Figures 1C, 1B, S1B, Movie S1, S2, S6, S7.

Cell fixation and staining

Cells were fixed using 4% formaldehyde and 250mM sorbitol for 30 minutes before being washed twice with PBS. For actin and nuclei staining phalloidin (Figures 2A, 2C, 6C, S2A, S2B), cells were span down at 1,000 rpm for 3 min after fixation and washed again three times with PBS before adding 10 µl of Alexa Fluor 488–phalloidin (Invitrogen) and DAPI at a final concentration of 5 µg/mL to 5 µl of concentrated sample. For plasma membrane and cell wall staining (Figure S2C), cells were incubated for 10 minutes with FM4-64FX (Invitrogen) at a final concentration of 10µM from 100× DMSO diluted stock solution and Calcofluor white (Sigma-Aldrich) at a final concentration of 5 µg/ml from a 200× stock solution prior to fixation. Cells were then fixed as previously mentioned and concentrated before being disposed between slide and coverslip.

For figures 5A, S5A and S5B, cells were pre-grown at 12ºC for 48h prior to fixing every hour for a total of 14 hours.

Live microscopy and pharmacological inhibitors

For live-cell imaging (Figures 1C-1F, 2B, 6A, S1A, S1B, S1C, Movies S1, S2, S4-S7) saturated culture was diluted 300x in fresh marine broth medium 1X inside a µ-Slide 4 or 8 well slide (Ibidi) at time zero. To ensure oxygenation during the whole period of the experiment, the cover has been removed. To maintain the temperature at 12°C we used a P-Lab Tek (Pecon GmbH) Heating/Cooling system connected to a Lauda Ecoline E100 circulating water bath. To reduce light toxicity, we used a 495nm Long Pass Filter (FGL495M- ThorLabs). Kymographs of cells undergoing cellularization in Figure 1D were constructed in ImageJ v1.46 by drawing a 3-pixel-wide (0.39 µm) line crossing the center of each cell.

For plasma membrane live staining (Figure 2B, Movie S4, S5), FM4-64 (Invitrogen) at a final concentration of 10µM from 100× DMSO diluted stock solution was added after 58 hours of growth.

Treatment with pharmacological inhibitors was performed on 54 hours grown cells inside a µ-Slide 8 well slide (Ibidi) at 12 ºC and lasted for 24 hours during which live microscopy was performed. Latrunculin A (Sigma-Aldrich) was used at final concentration of 50 µM from a stock of 20 mM in DMSO. CK666 (Sigma-Aldrich) was used at a final concentration of 100 µM from a stock of 10mM in DMSO. SMIFH2 (Sigma-Aldrich) was used at a final concentration of 40 µM from a stock of 10mM in DMSO. Blebbistatin (Sigma-Aldrich) was used at a final concentration of 1.25 µM from a stock of 2.5mM in DMSO. MBC (Sigma-Aldrich) was used at final concentration of 130 µg/ml from a stock of 2.5 mg/ml in dimethyl sulfoxide (DMSO).

Image analysis

Image analysis was done using ImageJ software (version 1.52) (Schneider et al., 2012). For measurements of cell diameter in Figures 1E and S1A, we cropped movies to ensure having a single cell per movie. We then transformed the movies into binaries to ensure later segmentation. We then used particle analysis function in ImageJ with a circularity parameter set to 0.65-1 to quantify measure cell perimeter. As cells are spherical, we computed cell diameter as:

For quantification of fraction of cells in each stage of cellularization Figure S2B, we used the ObjectJ plugin in ImageJ (National Institutes of Health).

All Figures were assembled with Illustrator CC 2017 (Adobe).

References

Abu-Jamous, B., and Kelly, S. (2018). Clust: automatic extraction of optimal co-expressed gene clusters from gene expression data. Genome Biol. *19,* 172.
Adam, J.C., Pringle, J.R., and Peifer, M. (2000). Evidence for Functional Differentiation among Drosophila Septins in Cytokinesis and Cellularization. Mol. Biol. Cell *11*, 3123–3135.

Afshar, K., Stuart, B., and Wasserman, S.A. (2000). Functional analysis of the Drosophila diaphanous FH protein in early embryonic development. Development *127*, 1887–1897.

Alexa, A., Rahnenführer, J., and Lengauer, T. (2006). Improved scoring of functional groups from gene expression data by decorrelating GO graph structure. Bioinformatics *22*, 1600–1607.

Altschul, S.F., Gish, W., Miller, W., Myers, E.W., and Lipman, D.J. (1990). Basic local alignment search tool. J. Mol. Biol. *215*, 403–410.

Barter, R.L., and Yu, B. (2018). Superheat: An R Package for Creating Beautiful and Extendable Heatmaps for Visualizing Complex Data. J. Comput. Graph. Stat. *27*, 910–922.

Betz, W.J., Mao, F., and Smith, C.B. (1996). Imaging exocytosis and endocytosis. Curr. Opin. Neurobiol. *6*, 365–371.

Bolger, A.M., Lohse, M., and Usadel, B. (2014). Trimmomatic: A flexible trimmer for Illumina sequence data. Bioinformatics *30*, 2114–2120.

Bonner, J.T. (1998). The origins of multicellularity. Integr. Biol. *1*, 27–36.

Braet, F., De Zanger, R., Jans, D., Spector, I., and Wisse, E. (1996). Microfilament-disrupting agent latrunculin A induces and increased number of fenestrae in rat liver sinusoidal endothelial cells: Comparison with cytochalasin B. Hepatology *24*, 627–635.

Bråte, J., Adamski, M., Neumann, R.S., Shalchian-Tabrizi, K., and Adamska, M. (2015). Regulatory RNA at the root of animals: dynamic expression of developmental lincRNAs in the calcisponge *Sycon ciliatum*. Proc. R. Soc. B Biol. Sci. *282*, 20151746.

Bray, N.L., Pimentel, H., Melsted, P., and Pachter, L. (2016). Near-optimal probabilistic RNA-seq quantification. Nat. Biotechnol. *34*, 525–527.

Brunet, T., and King, N. (2017). The Origin of Animal Multicellularity and Cell Differentiation. Dev. Cell *43*, 124–140.

Castagnetti, S., Novak, B., and Nurse, P. (2007). Microtubules offset growth site from the cell centre in fission yeast. J. Cell Sci. *120*, 2205–2213.

Cooper, J.A., and Kiehart, D.P. (1996). Septins may form a ubiquitous family of cytoskeletal filaments. J. Cell Biol. *134*, 1345–1348.

Csuros, M. (2010). Count: evolutionary analysis of phylogenetic profiles with parsimony and likelihood. Bioinformatics *26*, 1910–1912.

Dickinson, D.J., Nelson, W.J., and Weis, W.I. (2011). A Polarized Epithelium Organized by predates cadherin and catenin metazoan origins. *1*, 1336–1340.

Dickinson, D.J., Nelson, W.J., and Weis, W.I. (2012). An epithelial tissue in Dictyostelium challenges the traditional origin of metazoan multicellularity. BioEssays *34*, 833–840.

Dobin, A., Davis, C.A., Schlesinger, F., Drenkow, J., Zaleski, C., Jha, S., Batut, P., Chaisson, M., and Gingeras, T.R. (2012). STAR: ultrafast universal RNA-seq aligner. Bioinformatics *29*, 15–21.

Domazet-Lošo, T., and Tautz, D. (2010). A phylogenetically based transcriptome age index mirrors ontogenetic divergence patterns. Nature *468*, 815–819.

Eilbeck, K., Lewis, S.E., Mungall, C.J., Yandell, M., Stein, L., Durbin, R., and Ashburner, M. (2005). The Sequence Ontology: a tool for the unification of genome annotations. Genome Biol *6*, R44.

Emms, D.M., and Kelly, S. (2015). OrthoFinder: solving fundamental biases in whole genome comparisons dramatically improves orthogroup inference accuracy. Genome Biol. *16*, 1–14.

Farrell, J.A., and O'Farrell, P.H. (2014). From Egg to Gastrula: How the Cell Cycle Is Remodeled During the *Drosophila* Mid-Blastula Transition. Annu. Rev. Genet. *48*, 269–294.

Gaiti, F., Fernandez-Valverde, S.L., Nakanishi, N., Calcino, A.D., Yanai, I., Tanurdzic, M., and Degnan, B.M. (2015). Dynamic and widespread lncRNA expression in a sponge and the origin of animal complexity. Mol. Biol. Evol. *32*, 2367–2382.

Giansanti, M.G., Bonaccorsi, S., Williams, B., Williams, E. V., Santolamazza, C., Goldberg, M.L., and Gatti, M. (1998). Cooperative interactions between the central spindle and the contractile ring during Drosophila cytokinesis. Genes Dev. *12*, 396–410.

Grabherr, M.G., Haas, B.J., Yassour, M., Levin, J.Z., Thompson, D.A., Amit, I., Adiconis, X., Fan, L., Raychowdhury, R., Zeng, Q., et al. (2011). Full-length transcriptome assembly from RNA-Seq data without a reference genome. Nat. Biotechnol. *29*, 644–652.

Grau-bové, X., Ruiz-Trillo, I., and Irimia, M. (2018). Origin of exon skipping-rich transcriptomes in animals driven by evolution of gene architecture. Genome Biology *19*, 135.

Grau-Bové, X., Torruella, G., Donachie, S., Suga, H., Leonard, G., Richards, T.A., and Ruiz-Trillo, I. (2017). Dynamics of genomic innovation in the unicellular ancestry of animals. Elife *6*, 1–35.

Gunsalus, K.C., Bonaccorsi, S., Williams, E., Verni, F., Gatti, M., and Goldberg, M.L. (1995). Mutations in twinstar, a Drosophila gene encoding a cofilin/ADF homologue, result in defects in centrosome migration and cytokinesis. J. Cell Biol. *131*, 1243–1259.

Haas, B.J., Delcher, A.L., Mount, S.M., Wortman, J.R., Smith, R.K., Hannick, L.I., Maiti, R., Ronning, C.M., Rusch, D.B., Town, C.D., et al. (2003). Improving the Arabidopsis genome annotation using maximal transcript alignment assemblies. Nucleic Acids Res. *31*, 5654–5666.

Haas, B.J., Papanicolaou, A., Yassour, M., Grabherr, M., Blood, P.D., Bowden, J., Couger, M.B., Eccles, D., Li, B., Lieber, M., et al. (2013). De novo transcript sequence reconstruction from RNA-seq using the Trinity platform for reference generation and analysis. Nat. Protoc. *8*, 1494–1512.

Hehenberger, E., Kradolfer, D., and Kohler, C. (2012). Endosperm cellularization defines an important developmental transition for embryo development. Development *139*, 2031–2039.

Hetrick, B., Han, M.S., Helgeson, L.A., and Nolen, B.J. (2013). Small molecules CK-666 and CK-869 inhibit actin-related protein 2/3 complex by blocking an activating conformational change. Chem. Biol. *20*, 701–712.

Hezroni, H., Koppstein, D., Schwartz, M.G., Avrutin, A., Bartel, D.P., and Ulitsky, I. (2015). Principles of Long Noncoding RNA Evolution Derived from Direct Comparison of Transcriptomes in 17 Species. Cell Rep. *11*, 1110–1122.

Hoff, K.J., Lomsadze, A., Stanke, M., and Borodovsky, M. (2018). BRAKER2: Incorporating Protein Homology Information into Gene Prediction with GeneMark-EP and AUGUSTUS. Plant and Animal Genomes XXVI, January 14th 2018.

Huerta-Cepas, J., Forslund, K., Coelho, L.P., Szklarczyk, D., Jensen, L.J., von Mering, C., and Bork, P. (2017). Fast Genome-Wide Functional Annotation through Orthology Assignment by eggNOG-Mapper. Mol. Biol. Evol. *34*, 2115–2122.

Hunter, C., and Wieschaus, E. (2000). Regulated expression of nullo is required for the formation of distinct apical and basal adherens junctions in the Drosophila blastoderm. J. Cell Biol. *150*, 391–401.

Kalvari, I., Argasinska, J., Quinones-Olvera, N., Nawrocki, E.P., Rivas, E., Eddy, S.R., Bateman, A., Finn, R.D., and Petrov, A.I. (2017). Rfam 13.0: shifting to a genome-centric resource for non-coding RNA families. Nucleic Acids Res. *46*, D335–D342.

Kang, Y.-J., Yang, D.-C., Kong, L., Hou, M., Meng, Y.-Q., Wei, L., and Gao, G. (2017). CPC2: a fast and accurate coding potential calculator based on sequence intrinsic features. Nucleic Acids Res. *45*, W12–W16.

Keller, O., Kollmar, M., Stanke, M., and Waack, S. (2011). A novel hybrid gene prediction method employing protein multiple sequence alignments. Bioinformatics *27*, 757–763.

Kent, W.J. (2002). BLAT - The BLAST-like alignment tool. Genome Res. *12*, 656–664.

Kim, D., Langmead, B., and Salzberg, S.L. (2015a). HISAT: A fast spliced aligner with low memory requirements. Nat. Methods *12*, 357–360.

Kim, H.C., Jo, Y.J., Kim, N.H., and Namgoong, S. (2015b). Small molecule inhibitor of formin homology 2 domains (SMIFH2) reveals the roles of the formin family of proteins in spindle assembly and asymmetric division in mouse oocytes. PLoS One *10*, 1–15.

Kovács, M., Tóth, J., Hetényi, C., Málnási-Csizmadia, A., and Sellers, J.R. (2004). Mechanism of Blebbistatin Inhibition of Myosin II. J. Biol. Chem. *279*, 35557–35563.

Lawrence, M., Huber, W., Pagès, H., Aboyoun, P., Carlson, M., Gentleman, R., Morgan, M.T., and Carey, V.J. (2013). Software for Computing and Annotating Genomic Ranges. PLoS Comput. Biol. *9*, 1–10.

Leys, S.P., Nichols, S.A., and Adams, E.D.M. (2009). Epithelia and integration in sponges. Integr. Comp. Biol. *49*, 167–177.

Lomsadze, A., Ter-Hovhannisyan, V., Chernoff, Y.O., and Borodovsky, M. (2005). Gene identification in novel eukaryotic genomes by self-training algorithm. Nucleic Acids Res. *33*, 6494–6506.

Marshall, W.L., and Berbee, M.L. (2011). Facing Unknowns: Living cultures (Pirum gemmata gen. nov., sp. nov., and Abeoforma whisleri, gen. nov., sp. nov.) from invertebrate digestive tracts represent an undescribed clade within the unicellular opisthokont lineage ichthyosporea (Mesomycetozoea). Protist *162*, 33–57.

Marshall, W.L., and Berbee, M.L. (2013). Comparative morphology and genealogical delimitation of cryptic species of sympatric isolates of Sphaeroforma (Ichthyosporea, Opisthokonta). Protist *164*, 287–311.

Mazumdar, A., and Mazumdar, M. (2002). How one becomes many: Blastoderm cellularization in Drosophila melanogaster. BioEssays *24*, 1012–1022.

McLaren, W., Gil, L., Hunt, S.E., Riat, H.S., Ritchie, G.R.S., Thormann, A., Flicek, P., and Cunningham, F. (2016). The Ensembl Variant Effect Predictor. Genome Biol. *17*, 1–14.

Mendoza, L., Taylor, J.W., and Ajello, L. (2002). The class mesomycetozoea: a heterogeneous group of microorganisms at the animal-fungal boundary. Annu. Rev. Microbiol. *56*, 315–344.

de Mendoza, A., Suga, H., Permanyer, J., Irimia, M., and Ruiz-Trillo, I. (2015). Complex transcriptional regulation and independent evolution of fungal-like traits in a relative of animals. Elife *4*, e08904.

Miller, P.W., Clarke, D.N., Weis, W.I., Lowe, C.J., and Nelson, W.J. (2013). The evolutionary origin of epithelial cell-cell adhesion mechanisms. Curr. Top. Membr. *72*, 267-311.

Murray, P.S., and Zaidel-Bar, R. (2014). Pre-metazoan origins and evolution of the cadherin adhesome. Biol. Open *3*, 1183–1195.

Nurk, S., Bankevich, A., Antipov, D., Gurevich, A.A., Korobeynikov, A., Lapidus, A., Prjibelski, A.D., Pyshkin, A., Sirotkin, A., Sirotkin, Y., et al. (2013). Assembling Single-Cell Genomes and Mini-Metagenomes From Chimeric MDA Products. J. Comput. Biol. *20*, 714–737.

Ondracka, A., Dudin, O., and Ruiz-Trillo, I. (2018). Decoupling of Nuclear Division Cycles and Cell Size during the Coenocytic Growth of the Ichthyosporean Sphaeroforma arctica. Curr. Biol. *28*, 1964–1969.e2.

Parfrey, L.W., Lahr, D.J.G., Knoll, A.H., and Katz, L.A. (2011). Estimating the timing of early eukaryotic diversification with multigene molecular clocks. Proc. Natl. Acad. Sci. *108*, 13624–13629.

Patro, R., Duggal, G., Love, M.I., Irizarry, R.A., and Kingsford, C. (2017). Salmon provides fast and bias-aware quantification of transcript expression. Nat. Methods *14*, 417–419.

Pignocchi, C., Minns, G.E., Nesi, N., Koumproglou, R., Kitsios, G., Benning, C., Lloyd, C.W., Doonan, J.H., and Hills, M.J. (2009). ENDOSPERM DEFECTIVE1 Is a Novel Microtubule-Associated Protein Essential for Seed Development in Arabidopsis. Plant Cell *21*, 90–105.

Quinlan, A.R., and Hall, I.M. (2010). BEDTools: A flexible suite of utilities for comparing genomic features. Bioinformatics *26*, 841–842.

Quint, M., Drost, H.G., Gabel, A., Ullrich, K.K., Bönn, M., and Grosse, I. (2012). A transcriptomic hourglass in plant embryogenesis. Nature *490*, 98–101.

Richter, D.J., Fozouni, P., Eisen, M.B., and King, N. (2018). Gene family innovation, conservation and loss on the animal stem lineage. Elife *7*, 1–43.

Rodriguez-Boulan, E., and Macara, I.G. (2014). Organization and execution of the epithelial polarity programme. Nat. Rev. Mol. Cell Biol. *15*, 225–242.

Royou, A., Sullivan, W., and Karess, R. (2002). Cortical recruitment of nonmuscle myosin II in early syncytial Drosophila embryos . J. Cell Biol. *158*, 127–137.

Schneider, C.A., Rasband, W.S., and Eliceiri, K.W. (2012). NIH Image to ImageJ: 25 years of image analysis. Nat. Methods *9*, 671–675.

Sorensen, M.B. (2002). Cellularisation in the endosperm of Arabidopsis thaliana is coupled to mitosis and shares multiple components with cytokinesis. Development *129*, 5567–5576.

Stevenson, V., Hudson, A., Cooley, L., and Theurkauf, W.E. (2002). Arp2/3-dependent psuedocleavage furrow assembly in syncytial Drosophila embryos. Curr. Biol. *12*, 705–711.

Suga, H., and Ruiz-Trillo, I. (2013). Development of ichthyosporeans sheds light on the origin of metazoan multicellularity. Dev. Biol. *377*, 284–292.

Trincado, J.L., Entizne, J.C., Hysenaj, G., Singh, B., Skalic, M., Elliott, D.J., and Eyras, E. (2018). SUPPA2: Fast, accurate, and uncertainty-aware differential splicing analysis across multiple conditions. Genome Biol. *19*, 1–11.

Walker, B.J., Abeel, T., Shea, T., Priest, M., Abouelliel, A., Sakthikumar, S., Cuomo, C.A., Zeng, Q., Wortman, J., Young, S.K., et al. (2014). Pilon: An integrated tool for comprehensive microbial variant detection and genome assembly improvement. PLoS One *9*.

Wang, F., Dumstrei, K., Haag, T., and Hartenstein, V. (2004). The role of DE-cadherin during cellularization, germ layer formation and early neurogenesis in the Drosophila embryo. Dev. Biol. *270*, 350–363.

Whisler, H.C. (1968). Developmental Control of Amoebidium parasiticurn Amoeba - cyst In tryptone medium In daphnid extract. Dev. Biol. *17*, 562–570.

Wu, T.D., and Watanabe, C.K. (2005). GMAP: A genomic mapping and alignment program for mRNA and EST sequences. Bioinformatics *21*, 1859–1875.

Xue, W., Li, J.-T., Zhu, Y.-P., Hou, G.-Y., Kong, X.-F., Kuang, Y.-Y., and Sun, X.-W. (2013). L_RNA_scaffolder: scaffolding genomes with transcripts. BMC Genomics *14*, 604

Figure 1

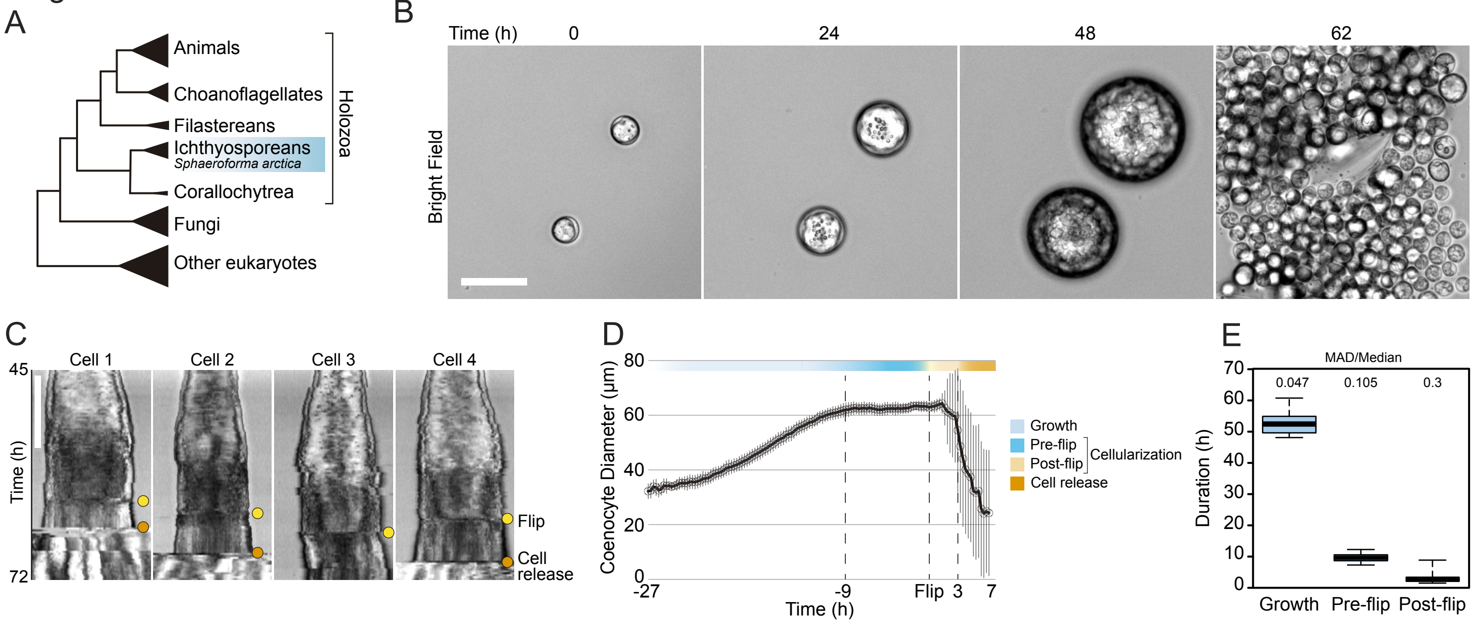

Figure 1. Cellularization dynamics in *Sphaeroforma arctica*

(A) Phylogenetic position of the ichthyosporean *Sphaeroforma arctica* in the tree of life

(B) Time-lapse images of the life-cycle of *S. arctica* show cell-size increase prior to cellularization and release of new-born cells. Associated with Movie S2. Bar, 50µm.

(C) Kymographs of 4 distinct cells undergoing cellularization with the time of flip (yellow) and cell release (orange) indicated for each. Bar, 50µm.

(D) Cell diameter over time of 65 single cell traces aligned to Flip reveals distinct cell stages: Growth, Pre and post-flip and cell release.

(E) Duration of growth, cellularization and post-flip represented as box-plots (N°cells > 100). MAD (Median absolute deviation) over median is used as a measure of variability.

Figure 2

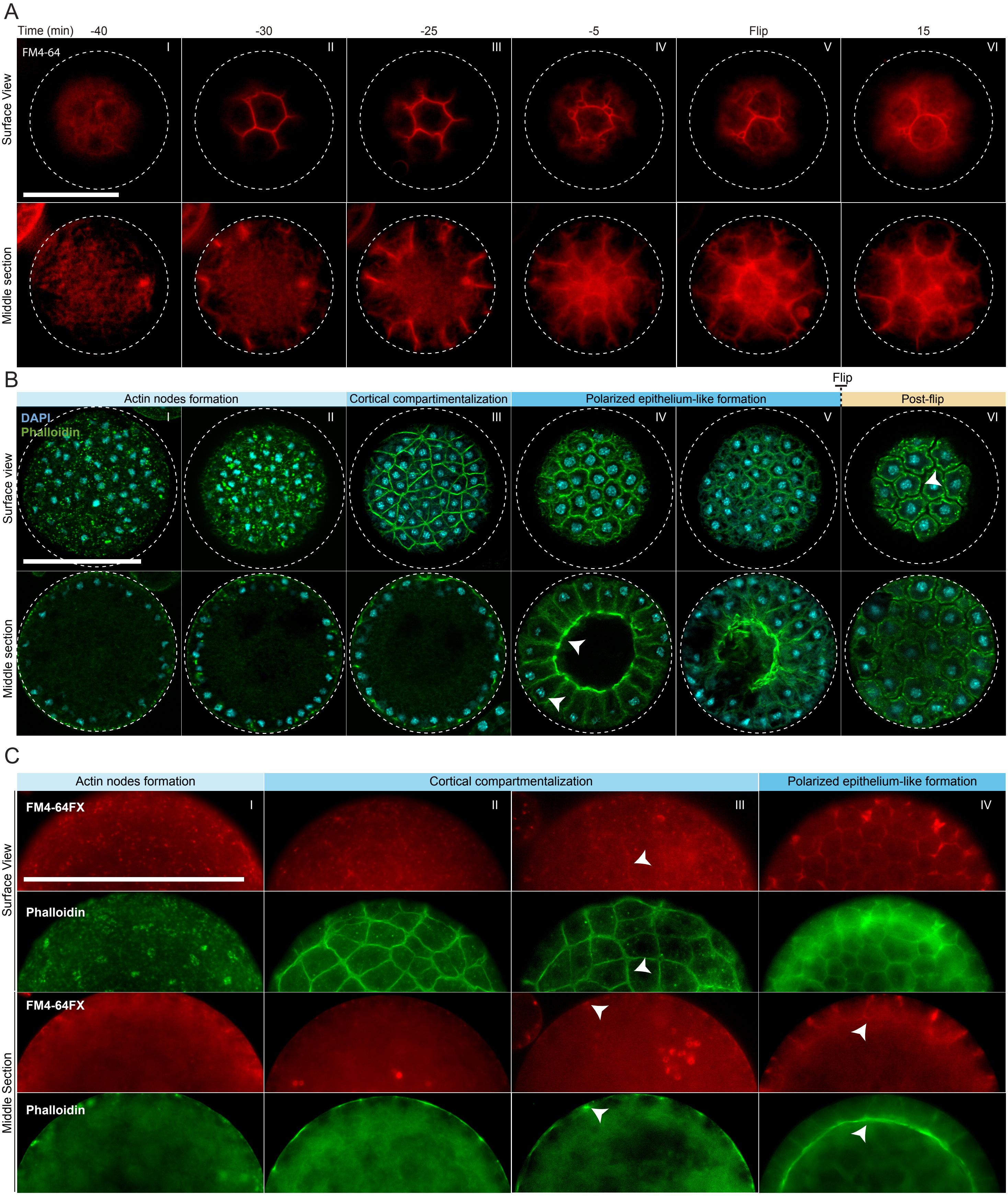

Figure 2. Actin cytoskeleton and plasma membrane dynamics during cellularization of *S. arctica*
(A) Dynamics of plasma membrane invaginations during cellularization. Live-cells, pre-grown for 58 hours, were stained with FM4-64 (10μM) and imagedusing epifluorescent microscopy with a 5 minutes interval. Bar, 50μm.
(B) Spatio-temporal organization of the actin cytoskeleton, nuclei and cells during cellularization. Synchronized cells of *S. arctica*, pre-grown for 48 hours, were fixed every hour for 14 hours and stained with phalloidin and DAPI to reveal cytoskeletal dynamics during cellularization. All cells were imaged using confocal microscopy.In panel IV, arrows indicate higher actin signal intensity on the internal side and that nuclei are localized close to the cortex indicating that the epithelium-like layer of cells is polarized. In panel VI, an arrow indicate that cells are apart from each other after flip. Bar, 50μm.
(C) Actin network is established prior to plasma membrane invaginations. Synchronized cells of *S. arctica*, pre-grown for 54 hours, were fixed every 2 hours for 10 hours and stained with both the membrane dye FM4-64FX and phalloidin. Arrows show sites of colocalization between both markers at the onset of plasma membrane invaginations. Bar, 50μm.

Figure 3

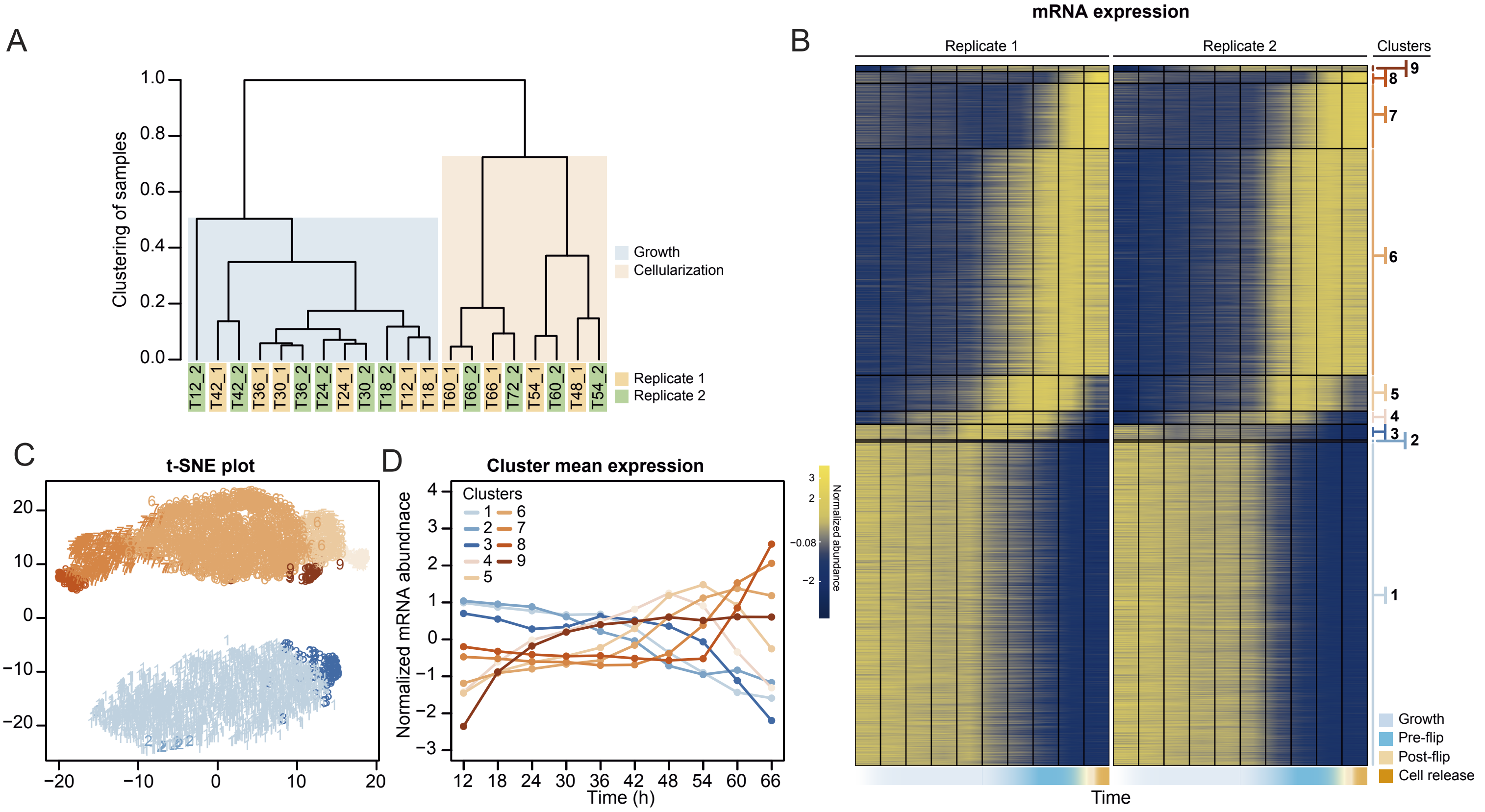

Figure 3. Transcriptional dynamics across the *S. arctica* life cycle

(A) Hierarchical clustering of time point samples by Euclidian distance of spearman correlation coefficient. The sample T48_2 is missing due to technical reason.

(B) A heatmap of 4,441 coding genes that were clustered into 9 clusters.

(C) A t-SNE plot of clustered genes.

(D) Mean expression profile of each gene expression cluster.

Figure 4

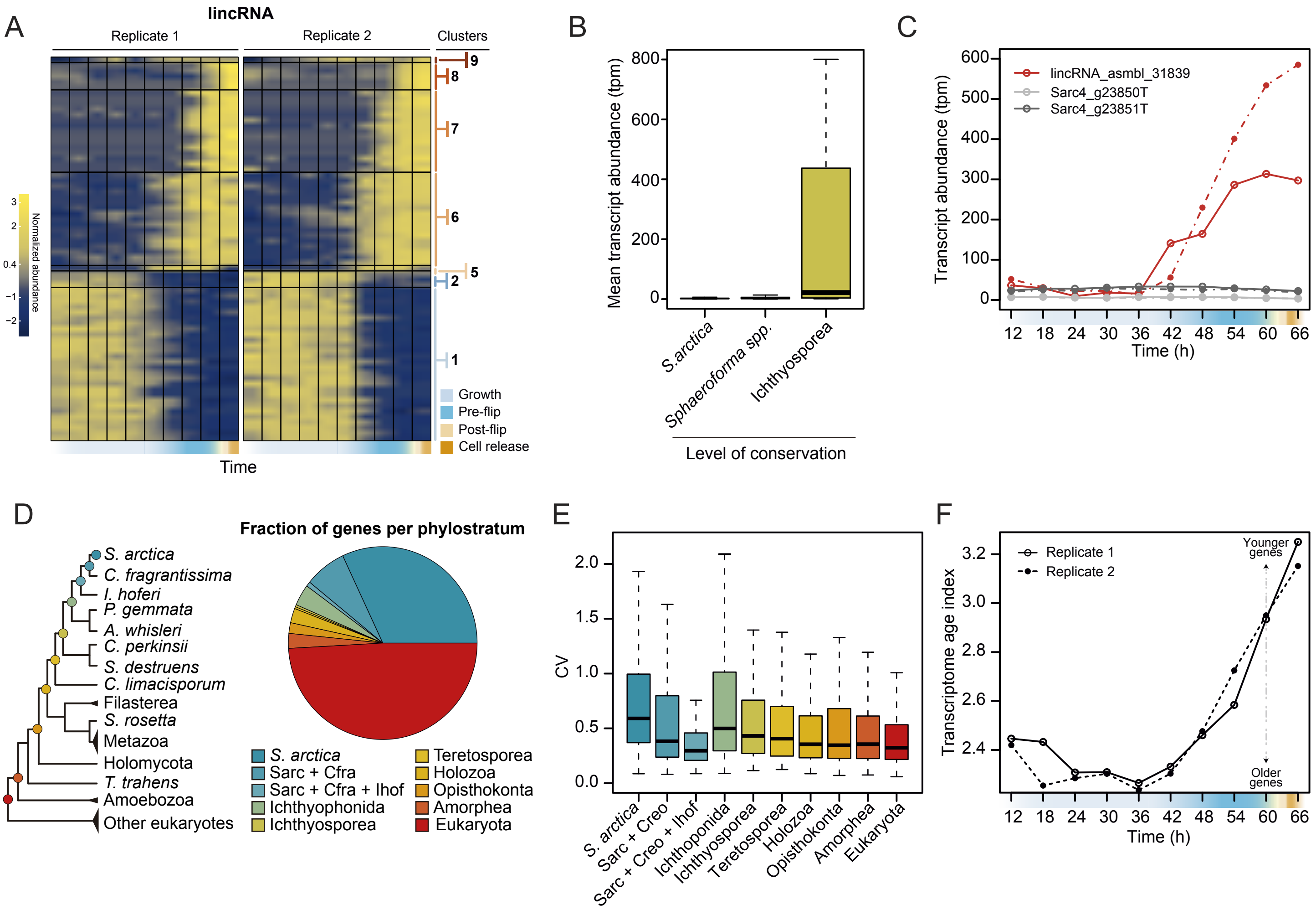

Figure 4. Dynamics of lincRNAs, alternative splicing, and gene phylostrata

(A) A heatmap of 70 long intergenic non-coding RNAs (lincRNAs) that co-cluster with coding genes.

(B) mean expression level of the lincRNAs, binned by degree of conservation.

(C) Expression of the conserved lincRNA, lincRNA: asmbl_31839 and the two coding genes located immediately upstream and downstream of it.

(D) A phylogenetic tree indicating the 10 defined phylostrata, and a pie chart of fractions of all expressed genes per phylostratum

(E) Coefficient of variance of gene expression across the *S. arctica* life cycle, binned by phylostratum

(F) Transcriptome age index for the *S. arctica* life cycle

Figure 5

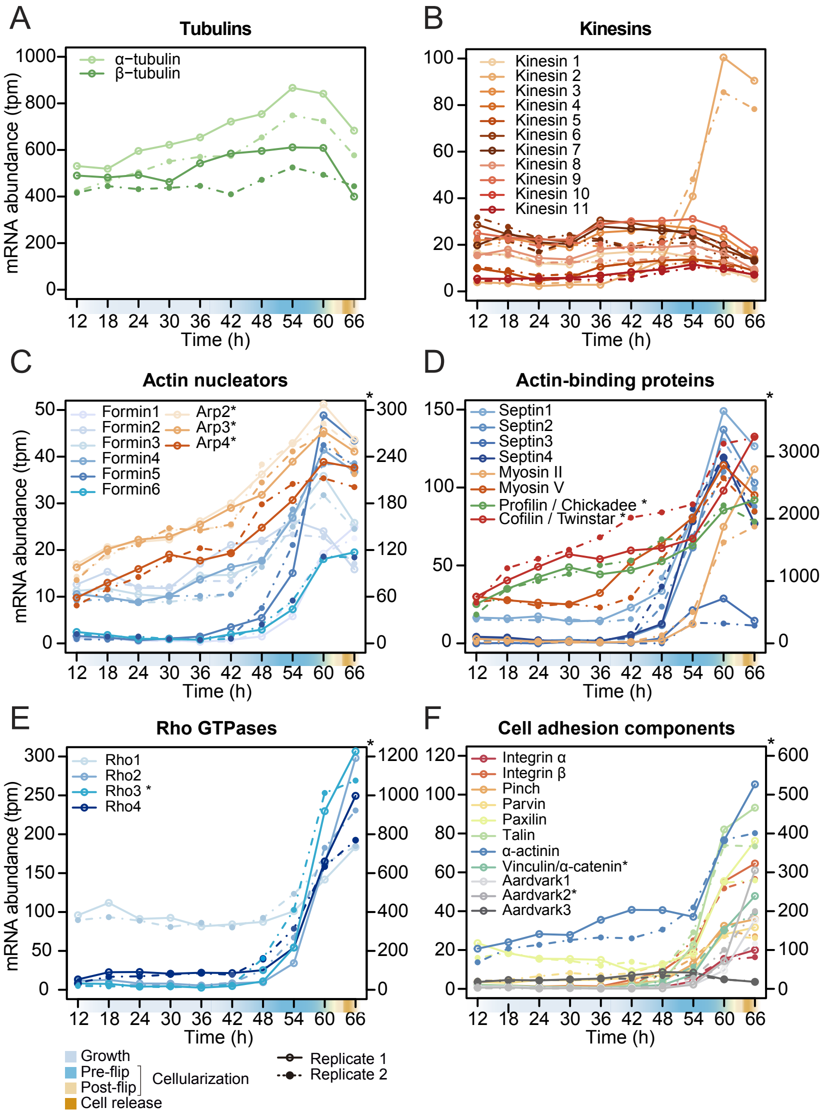

Figure 5. Temporal transcript abundance of cytoskeletal, cell polarity and cell adhesion genes

(A-F) Gene expression of indicated genes across the *S. arctica* life cycle

Figure 6

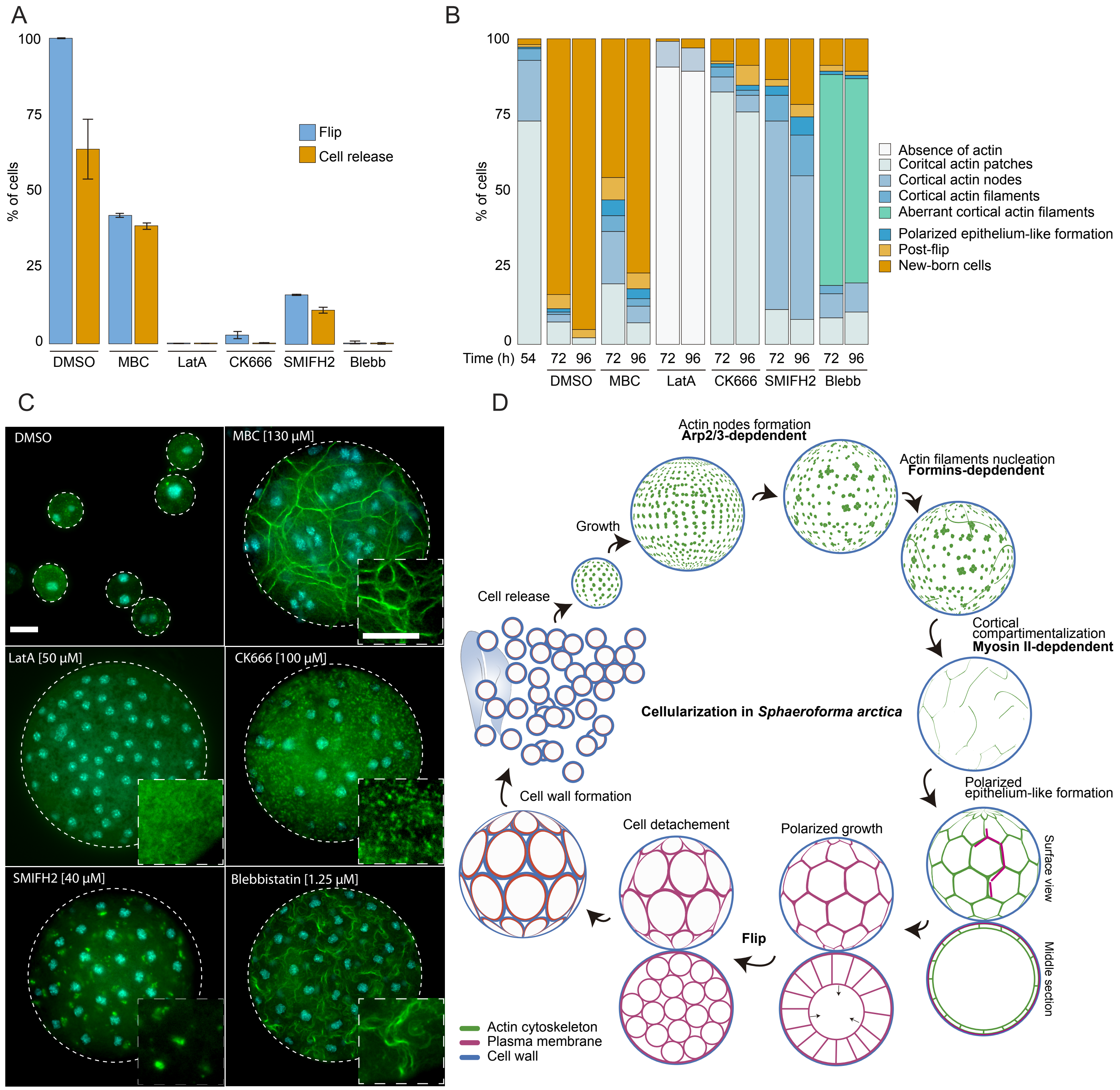

Figure 6. The actomyosin network organization is crucial for cellularization of *S. arctica*

(A) Depolymerization of microtubules and actin, as well as inhibition of Arp2/3, formins and myosin II affect “flip” and release of new born cells. Synchronized cells of *S. arctica*, pre-grown for 54 hours, were imaged for 24 hours in presence of multiple pharmacological inhibitors (DMSO as a control, MBC, Latrunculin A, CK666, SMIFH2, Blebbistatin). Cells undergoing flip and cell release throughout the duration of the experiment were measured (N>400 cells, Error bars are standard deviation from three independent experiments).

(B) Temporal functions of the Arp2/3 complex, formins and myosin II in distinct stages of cellularization. Synchronized cells of *S. arctica*, pre-grown for 54 hours were subject to multiple pharmacological inhibitors treatments (DMSO as a control, MBC, Latrunculin A, CK666, SMIFH2, Blebbistatin) and fixed and stained with phalloidin and DAPI after 24h and 48 hours of treatments. Phalloidin staining allows us to measure the fraction of cells exhibiting different actin and cellular structures throughout cellularization.

(C) The different actin structures observed when cells are treated with multiple pharmacological inhibitors treatments (DMSO as a control, MBC, Latrunculin A, CK666, SMIFH2, Blebbistatin). Bar, 10μm.

(D) A model representing the actin cytoskeleton, plasma membrane and cell wall at different stages of the cellularization process in *S. arctica*, indicating sequential steps of actin remodeling mediated by Arp2/3, formins and Myosin II.

Figure S1

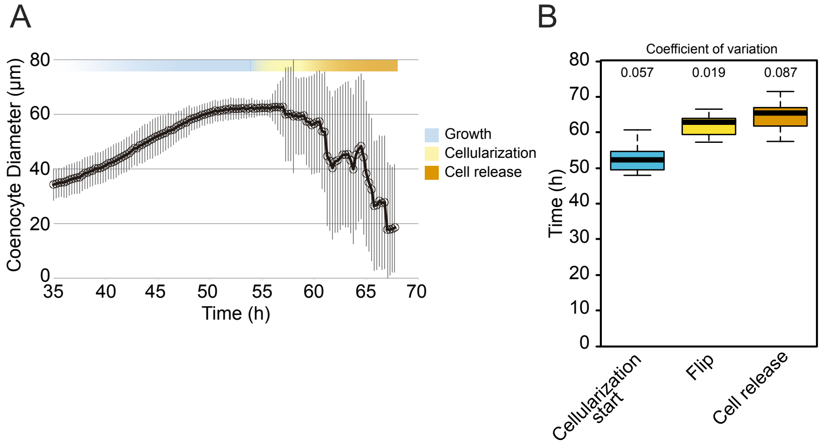

Figure S1.

(A) Cell diameter over time of 65 single cell traces aligned to time. Variability increases from 54h onwards due to asynchronous release of new born cells.

(B) The average time at which cells start cellularization,undergo flip or release new-born cells in a bulk culture. (N°cells = 100).

Figure S2

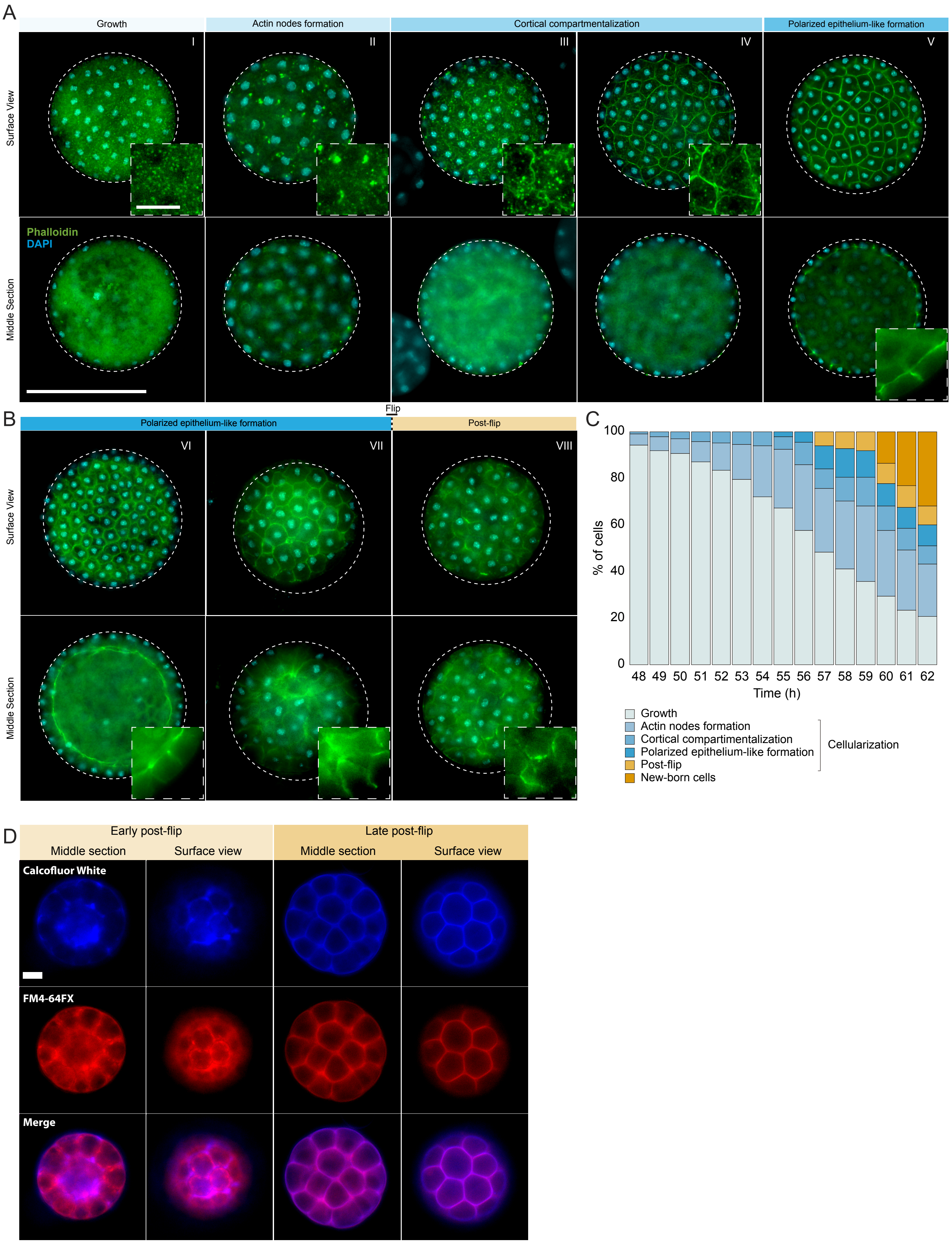

Figure S2.
(A) Epifluorescence microscopy images of the cellularization process using phalloidin and DAPI. Arrows show the different actin structures during the different stages of cellularization. Bars, 50μm for whole image and 10μm for the zoom.
(B) fraction of cells exhibiting different actin and cellular structures throughout cellularization. The temporal order of actin structures show that the stages occur sequentially. (N°cells = 300)
(C) Cell wall formation is observed only post-flip. Cells were fixed and co-stained with the membrane dye FM4-64FX and the cell-wall dye calcofluor white and imaged using an epifluorescence microscope. Bar, 10μm.

Figure S3

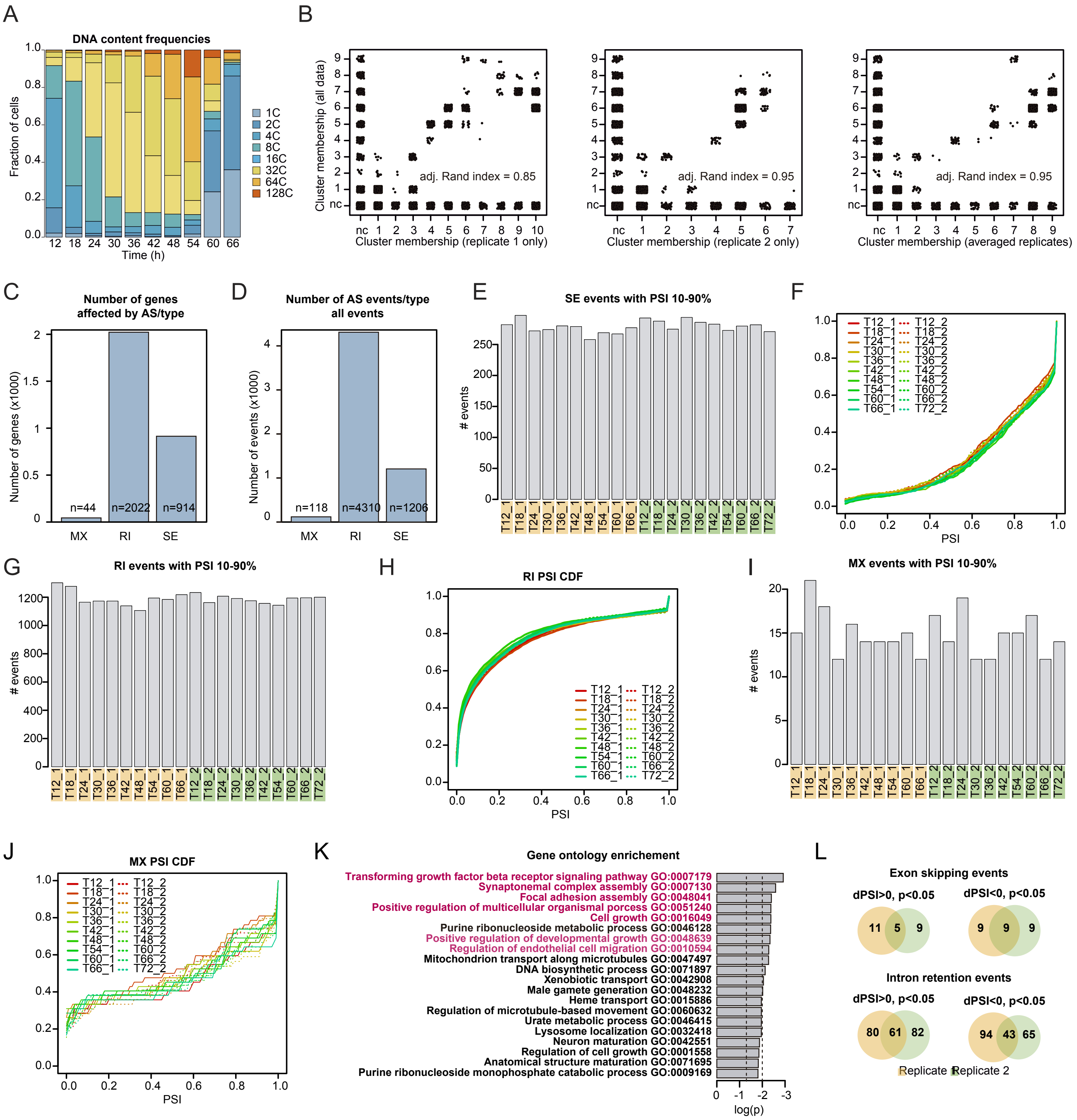

Figure S3.
(A) Distributions of nuclear content of *S. arctica* cells across the life cycle in the samples used for transcriptional profiling of a representative replicate, measured by flow cytometry.
(B) Cluster membership comparison of transcripts clustering with the entire dataset with samples from either replicate only or averaged abundances of both replicates. The figures and calculated adjusted Rand index demonstrate that cluster memberships are robust. nc - not clustered (genes were not included in either gene expression cluster).
(C) number of genes affected by the three types of alternative splicing. MX - mutually exclusive exons; RI - intron retention; SE - exon skipping.
(D) number of alternative splicing events. Labels same as in (C)
(E-J) Dynamics of alternative splicing across the *S. arctica* life cycle. Number of events per sample and cumulative distribution function (CDF) for exon skipping (SE), intron retention (RI) and mutually exclusive exons (MX).
(K) Gene ontology enrichment of genes affected by alternative splicing, calculated by elim method using Bonferroni correction
(L) Venn diagram of alternative splicing events that differ significantly between the growth and cellularization stage. dPSI - differential percentage spliced-in.

Figure S4

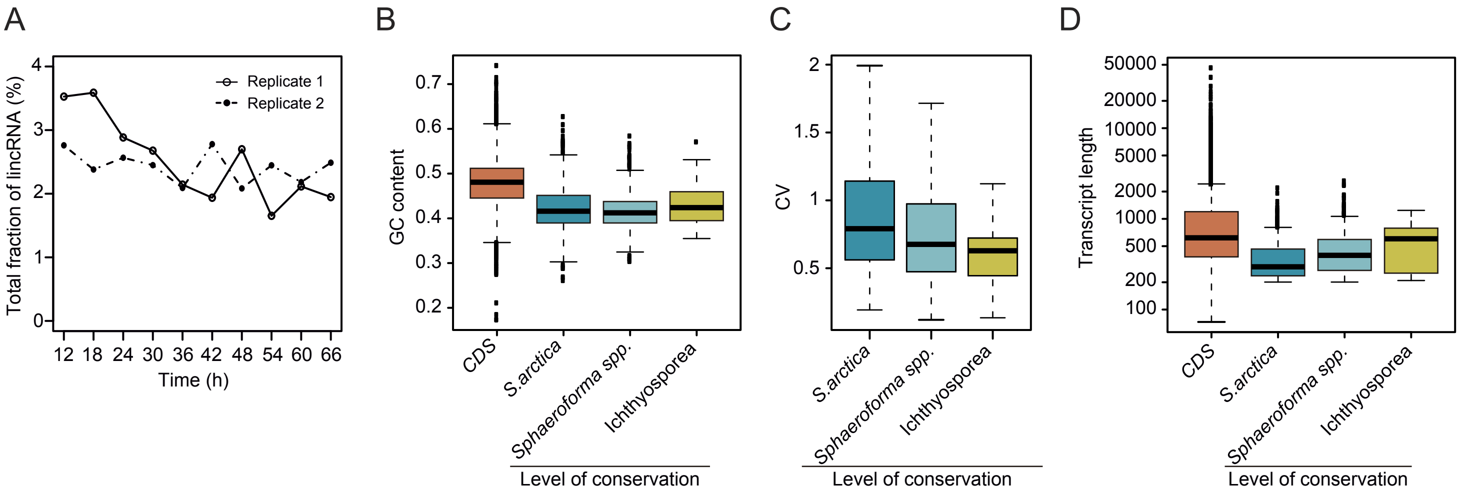

E

Sequence alignment of lincRNA: asmbl_31839 with homologs across Ichthyosporea

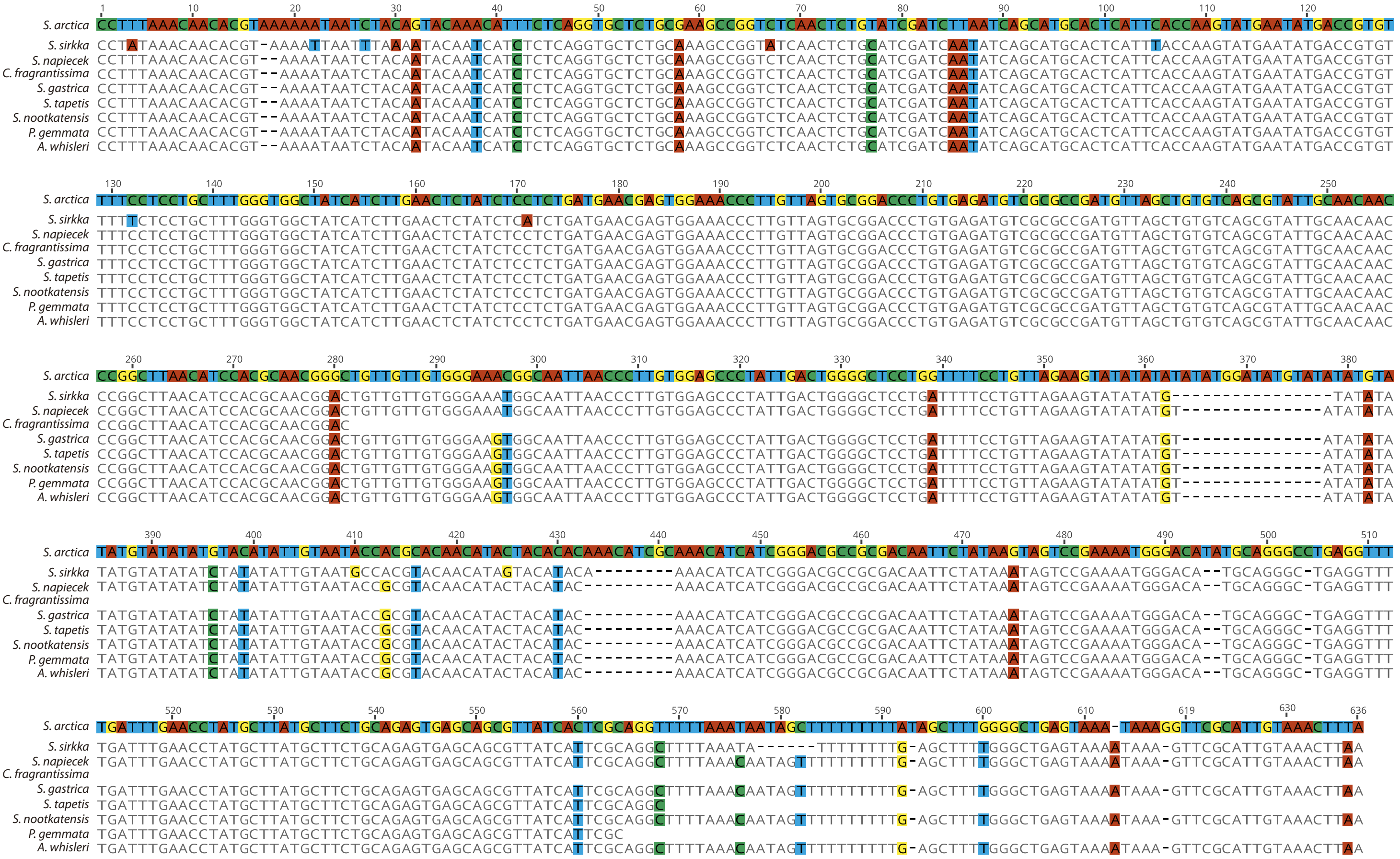

Figure S4.

(A) Fraction of total abundance of long intergenic non-coding RNA transcripts (lincRNAs) among all transcripts.

(B) Comparison of GC content of lincRNAs binned by degree of conservation with coding genes (CDS).

(C) Coefficient of variation of expression across the S. arctica life cycle of lincRNAs binned by degree of conservation.

(D) Transcript length of lincRNAs binned by degree of conservation and coding genes.

(E) Sequence alignment of lincRNA: asmbl_31839 with homologs across ichthyosporea.

Figure S5

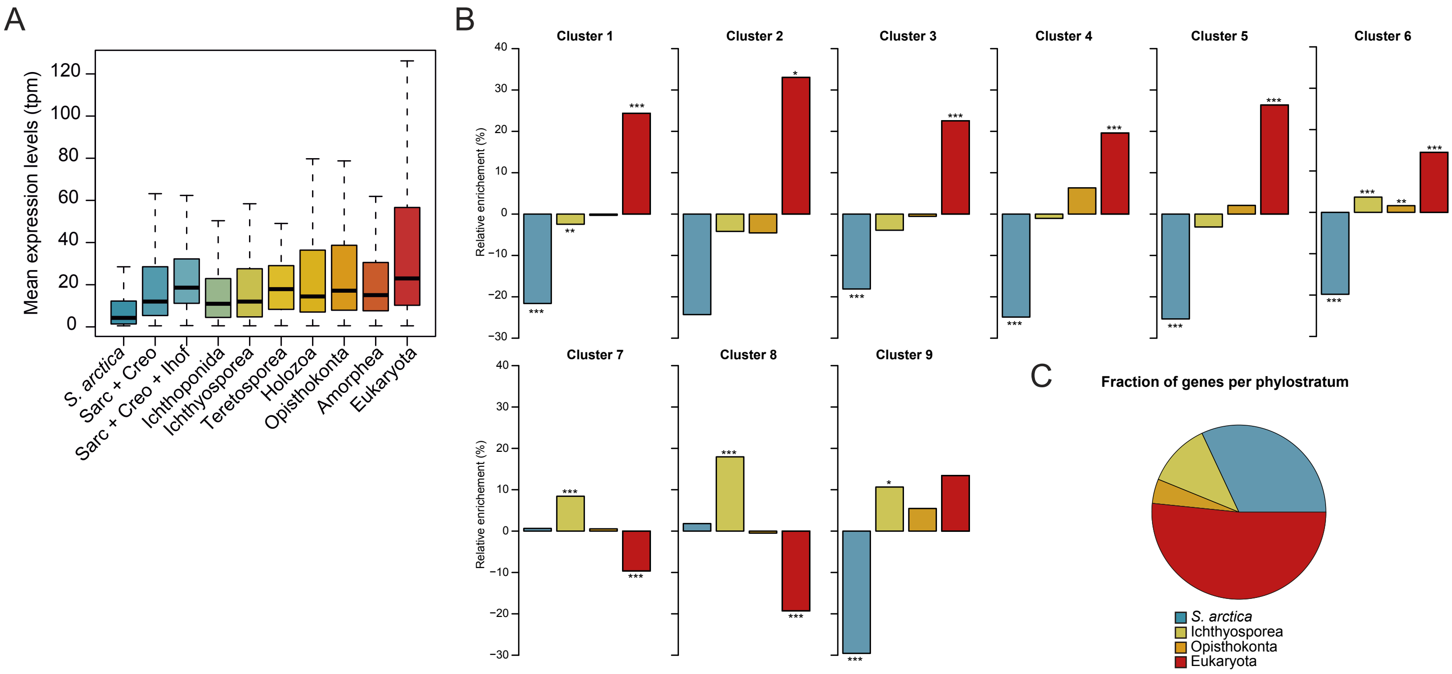

Figure S5.
(A) Mean gene expression across the *S. arctica* life cycle, binned by phylostratum.
(B) Relative enrichment of gene phylostrata in within gene expression clusters. Original 10 phylostrata were collapsed into 4.
(* - $p < 0.05$, ** - $p < 0.01$, *** - $p < 0.001$, Fisher exact test)
(C) Fraction of genes per phylostratum used in (B)

Figure S6

A

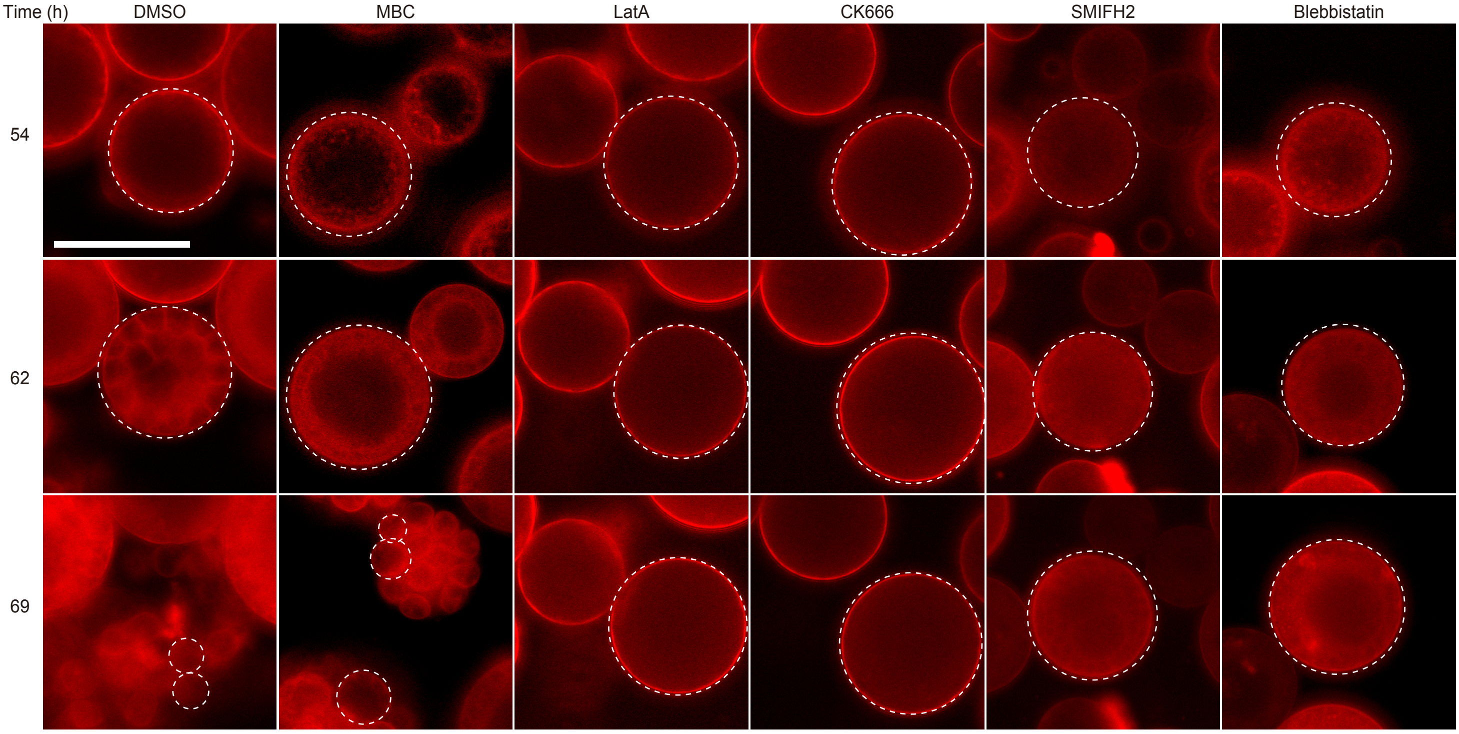

B

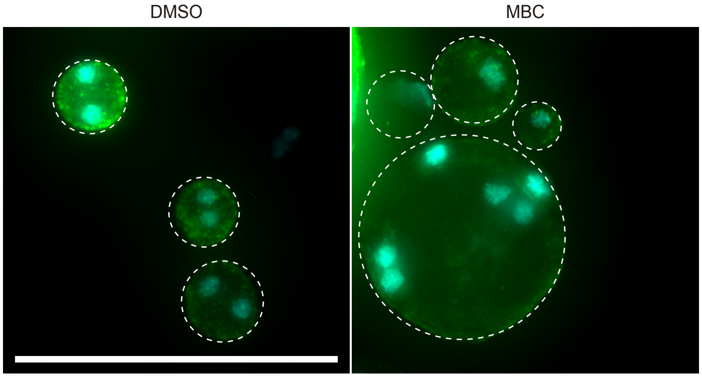

Figure S6.
(A) Depolymerization of microtubules and actin, as well as inhibition of Arp2/3, formins and myosin II affect plasma membrane invaginations. Synchronized cells of *S. arctica*, pre-grown for 54 hours, were imaged for 24 hours in presence of multiple pharmacological inhibitors (DMSO as a control, MBC, Latrunculin A, CK666, SMIFH2, Blebbistatin). Note the different delay in cell release and the cell size variability of new born cells after treatment with MBC. Bar, 50µm.
(B) Depolymerization of microtubules generates new-born cells with uneven size and number of nuclei. Synchronized cells of *S. arctica*, pre-grown for 54 hours, were imaged after 24 hours in presence MBC or DMSO. Note the different sizes and uneven number of nuclei of MBC-treated new born cells.

Table S1.

Metrics of the *S. arctica* genome assemblies

Metrics	Version 1 (Grau-Bove et al. 2017)	Version 2.1 (this study)
Total sequence length	121,588,341 bp	115,261,641 bp
Number of supercontigs	15,618	737
Supercontig N50	64,598 bp	243,943 bp
Longest supercontig	357,797 bp	776,519 bp

Metrics of the *S. arctica* genome assemblies (without the mitochondrial genome)

Metrics	Version 1 (Grau-Bove et al. 2017)	Version 2.1 (this study)
Total sequence length	121,588,341 bp	115,079,836 bp
Number of supercontigs	15,618	732
Supercontig N50	64,598 bp	244,210 bp
Longest supercontig	357,797 bp	776,519 bp

Table S2 **Gene ontology enrichement of expression clusters**

GO: ID	GO Term	p value
	Cluster 1	
GO:0040010	positive regulation of growth rate	2.5e-19
GO:0040035	hermaphrodite genitalia development	1.5e-13
GO:0006364	rRNA processing	6.5e-12
GO:0002119	nematode larval development	2.3e-11
GO:0006898	receptor-mediated endocytosis	1.4e-09
GO:0000398	mRNA splicing, via spliceosome	7.2e-07
GO:0006259	DNA metabolic process	1.5e-06
GO:0009792	embryo development ending in birth or egg hatching	2.6e-06
GO:0042254	ribosome biogenesis	8,00E-06
GO:0000381	regulation of alternative mRNA splicing, via spliceosome	8.4e-06
GO:0006626	protein targeting to mitochondrion	1.6e-05
GO:0030174	regulation of DNA-dependent DNA replication initiation	3.5e-05
GO:0030261	chromosome condensation	4.9e-05
GO:0040020	regulation of meiotic nuclear division	6.5e-05
GO:0051084	de novo' posttranslational protein folding	7.1e-05
GO:0022008	neurogenesis	8.5e-05
GO:0032201	telomere maintenance via semi-conservative replication	9.4e-05
GO:0006271	DNA strand elongation involved in DNA replication	1,00E-04
GO:0006412	translation	0.00016
GO:0006385	transcription elongation from RNA polymerase III promoter	0.00048
GO:0006386	termination of RNA polymerase III transcription	0.00048
GO:0017183	peptidyl-diphthamide biosynthetic process from peptidyl-histidine	0.00048
GO:0030488	tRNA methylation	0.00053
GO:0031167	rRNA methylation	0.00059
GO:0010833	telomere maintenance via telomere lengthening	0.00064
GO:0090305	nucleic acid phosphodiester bond hydrolysis	0.00065
GO:0006997	nucleus organization	0.00068
GO:0000731	DNA synthesis involved in DNA repair	0.00114
GO:0006418	tRNA aminoacylation for protein translation	0.00163
GO:0006369	termination of RNA polymerase II transcription	0.00174
GO:0016973	poly(A)+ mRNA export from nucleus	0.00193
GO:0006376	mRNA splice site selection	0.00193
GO:0006334	nucleosome assembly	0.00216
GO:0000466	maturation of 5.8S rRNA from tricistronic rRNA transcript (SSU-rRNA, 5.8S rRNA, LSU-rRNA)	0.00217
GO:0018992	germ-line sex determination	0.00217
GO:0019509	L-methionine salvage from methylthioadenosine	0.00221
GO:0009926	auxin polar transport	0.00221
GO:0007339	binding of sperm to zona pellucida	0.00221
GO:0009304	tRNA transcription	0.00221
GO:0006610	ribosomal protein import into nucleus	0.00221
GO:0043558	regulation of translational initiation in response to stress	0.00236
GO:0034969	histone arginine methylation	0.00236
GO:0009303	rRNA transcription	0.00267
GO:0022618	ribonucleoprotein complex assembly	0.00279
GO:0006406	mRNA export from nucleus	0.00293

GO:0000722	telomere maintenance via recombination	0.00297
GO:0030490	maturation of SSU-rRNA	0.00312
GO:0006595	polyamine metabolic process	0.00321
GO:0009113	purine nucleobase biosynthetic process	0.00321
GO:0032259	methylation	0.00404
GO:0044260	cellular macromolecule metabolic process	0.00408
GO:0048024	regulation of mRNA splicing, via spliceosome	0.00443
GO:0043928	exonucleolytic catabolism of deadenylated mRNA	0.00459
GO:0006268	DNA unwinding involved in DNA replication	0.00472
GO:0044743	protein transmembrane import into intracellular organelle	0.00481
GO:0034660	ncRNA metabolic process	0.00572
GO:0007076	mitotic chromosome condensation	0.00628
GO:0002183	cytoplasmic translational initiation	0.00677
GO:0042246	tissue regeneration	0.00677
GO:0000480	endonucleolytic cleavage in 5'-ETS of tricistronic rRNA transcript (SSU-rRNA, 5.8S rRNA, LSU-rRNA)	0.00677
GO:0000472	endonucleolytic cleavage to generate mature 5'-end of SSU-rRNA from (SSU-rRNA, 5.8S rRNA, LSU-rRNA)	0.00677
GO:0006284	base-excision repair	0.00743
GO:0007095	mitotic G2 DNA damage checkpoint	0.00873
GO:0001703	gastrulation with mouth forming first	0.00884
GO:0000469	cleavage involved in rRNA processing	0.009
GO:0007089	traversing start control point of mitotic cell cycle	0.00915
GO:0080034	host response to induction by symbiont of tumor, nodule or growth in host	0.00915
GO:0035247	peptidyl-arginine omega-N-methylation	0.00915
GO:0000470	maturation of LSU-rRNA	0.00915
GO:0009219	pyrimidine deoxyribonucleotide metabolic process	0.00915
GO:0031122	cytoplasmic microtubule organization	0.00965
GO:0040022	feminization of hermaphroditic germ-line	0.00965
GO:0006607	NLS-bearing protein import into nucleus	0.00965
GO:0000447	endonucleolytic cleavage in ITS1 to separate SSU-rRNA from 5.8S rRNA and LSU-rRNA from tricistronic r	0.00965
GO:0000460	maturation of 5.8S rRNA	0.00997
Cluster 2		
GO:1901671	positive regulation of superoxide dismutase activity	0.0018
GO:0048318	axial mesoderm development	0.0018
GO:0034463	90S preribosome assembly	0.0018
GO:0042474	middle ear morphogenesis	0.0073
GO:0006412	translation	0.0075
Cluster 3		
GO:0033120	positive regulation of RNA splicing	0.00044
GO:0000162	tryptophan biosynthetic process	0.00087
GO:0006777	Mo-molybdopterin cofactor biosynthetic process	0.00144
GO:0034508	centromere complex assembly	0.00144
GO:0032324	molybdopterin cofactor biosynthetic process	0.00298
GO:0045144	meiotic sister chromatid segregation	0.00298
GO:0006913	nucleocytoplasmic transport	0.0074
Cluster 4		
GO:0006145	purine nucleobase catabolic process	0,0011
GO:0006573	valine metabolic process	0,0024
GO:0042430	indole-containing compound metabolic process	0,003

GO:0031365	N-terminal protein amino acid modification	0,004
GO:0008593	regulation of Notch signaling pathway	0,0041
GO:0055114	oxidation-reduction process	0,0041
GO:0009083	branched-chain amino acid catabolic process	0,0072
GO:0009072	aromatic amino acid family metabolic process	0,0085
Cluster 5		
GO:0006891	intra-Golgi vesicle-mediated transport	6.1e-05
GO:0019915	lipid storage	0.00028
GO:0046474	glycerophospholipid biosynthetic process	0.00046
GO:0051208	sequestering of calcium ion	9,00E-04
GO:0006890	retrograde vesicle-mediated transport, Golgi to endoplasmic reticulum	0.00115
GO:0048205	COPI coating of Golgi vesicle	0.00116
GO:0007030	Golgi organization	0.00126
GO:0016185	synaptic vesicle budding from presynaptic endocytic zone membrane	0.00239
GO:0035158	regulation of tube diameter, open tracheal system	0.00241
GO:0044106	cellular amine metabolic process	0.00269
GO:0019884	antigen processing and presentation of exogenous antigen	0.00289
GO:0010883	regulation of lipid storage	0.00321
GO:0006901	vesicle coating	0.0039
GO:0002474	antigen processing and presentation of peptide antigen via MHC class I	0.0042
GO:0030536	larval feeding behavior	0.00472
GO:0046487	glyoxylate metabolic process	0.00472
GO:0035149	lumen formation, open tracheal system	0.00472
GO:0072578	neurotransmitter-gated ion channel clustering	0.00472
GO:0048079	regulation of cuticle pigmentation	0.00472
GO:0032075	positive regulation of nuclease activity	0.00511
GO:0019886	antigen processing and presentation of exogenous peptide antigen via MHC class II	0.00511
GO:0015908	fatty acid transport	0.00534
GO:0030258	lipid modification	0.00753
GO:0050690	regulation of defense response to virus by virus	0.00772
GO:0034629	cellular protein-containing complex localization	0.00772
GO:0007286	spermatid development	0.00775
GO:0045807	positive regulation of endocytosis	0.00775
GO:0032101	regulation of response to external stimulus	0.00936
GO:0044070	regulation of anion transport	0.00983
Cluster 6		
GO:0008360	regulation of cell shape	1.7e-05
GO:0061024	membrane organization	3.4e-05
GO:0019226	transmission of nerve impulse	4.6e-05
GO:0016197	endosomal transport	4.6e-05
GO:0030833	regulation of actin filament polymerization	5.5e-05
GO:0048011	neurotrophin TRK receptor signaling pathway	5.5e-05
GO:0008543	fibroblast growth factor receptor signaling pathway	0.00013
GO:0060341	regulation of cellular localization	0.00013
GO:0019228	neuronal action potential	0.00016
GO:0007015	actin filament organization	2,00E-04
GO:0007173	epidermal growth factor receptor signaling pathway	0.00021
GO:0030163	protein catabolic process	0.00021

GO:0006821	chloride transport	0.00024
GO:0035023	regulation of Rho protein signal transduction	0.00028
GO:0043547	positive regulation of GTPase activity	0.00031
GO:0007110	meiosis I cytokinesis	0.00034
GO:0007111	meiosis II cytokinesis	0.00034
GO:0016080	synaptic vesicle targeting	0.00035
GO:0042552	myelination	0.00052
GO:0007268	chemical synaptic transmission	0.00053
GO:0033121	regulation of purine nucleotide catabolic process	0.00055
GO:0006928	movement of cell or subcellular component	6,00E-04
GO:1901615	organic hydroxy compound metabolic process	6,00E-04
GO:0051650	establishment of vesicle localization	0.00062
GO:0009118	regulation of nucleoside metabolic process	0.00065
GO:0006874	cellular calcium ion homeostasis	0.00074
GO:0007265	Ras protein signal transduction	0.00078
GO:0070588	calcium ion transmembrane transport	0.00083
GO:0032147	activation of protein kinase activity	0.00085
GO:0019886	antigen processing and presentation of exogenous peptide antigen via MHC class II	0.00095
GO:0048259	regulation of receptor-mediated endocytosis	0.00096
GO:0044089	positive regulation of cellular component biogenesis	0.00098
GO:0007409	axonogenesis	0.00113
GO:0051046	regulation of secretion	0.0012
GO:0030155	regulation of cell adhesion	0.00123
GO:0034314	Arp2/3 complex-mediated actin nucleation	0.00151
GO:0031018	endocrine pancreas development	0.00151
GO:0007031	peroxisome organization	0.00155
GO:0071242	cellular response to ammonium ion	0.00155
GO:0048193	Golgi vesicle transport	0.00164
GO:0048137	spermatocyte division	0.0018
GO:0048814	regulation of dendrite morphogenesis	0.0018
GO:0006487	protein N-linked glycosylation	0.00187
GO:0030031	cell projection assembly	0.0019
GO:0030855	epithelial cell differentiation	0.00194
GO:0000212	meiotic spindle organization	0.00198
GO:0000281	mitotic cytokinesis	0.00206
GO:0006635	fatty acid beta-oxidation	0.00206
GO:0042981	regulation of apoptotic process	0.00207
GO:0043161	proteasome-mediated ubiquitin-dependent protein catabolic process	0.00215
GO:0048666	neuron development	0.00219
GO:0046488	phosphatidylinositol metabolic process	0.00224
GO:0010565	regulation of cellular ketone metabolic process	0.00238
GO:0009968	negative regulation of signal transduction	0.00239
GO:0030242	autophagy of peroxisome	0.0025
GO:0051278	fungal-type cell wall polysaccharide biosynthetic process	0.0025
GO:0046325	negative regulation of glucose import	0.0025
GO:0035372	protein localization to microtubule	0.0025
GO:0060049	regulation of protein glycosylation	0.0025
GO:0016137	glycoside metabolic process	0.0025

GO:0035118	embryonic pectoral fin morphogenesis	0.0025
GO:0010256	endomembrane system organization	0.00252
GO:0032880	regulation of protein localization	0.00261
GO:0009617	response to bacterium	0.00273
GO:0050654	chondroitin sulfate proteoglycan metabolic process	0.00275
GO:0001707	mesoderm formation	0.00275
GO:1900544	positive regulation of purine nucleotide metabolic process	0.00275
GO:0051261	protein depolymerization	0.00291
GO:0007605	sensory perception of sound	0.00291
GO:0032506	cytokinetic process	0.00294
GO:0006023	aminoglycan biosynthetic process	0.00311
GO:0051289	protein homotetramerization	0.00311
GO:0051351	positive regulation of ligase activity	0.00331
GO:0051443	positive regulation of ubiquitin-protein transferase activity	0.00331
GO:0007626	locomotory behavior	0.00351
GO:0030010	establishment of cell polarity	0.00356
GO:0007112	male meiosis cytokinesis	0.00359
GO:0046135	pyrimidine nucleoside catabolic process	0.00359
GO:0030166	proteoglycan biosynthetic process	0.00359
GO:0019932	second-messenger-mediated signaling	0.00391
GO:0002479	antigen processing and presentation of exogenous peptide antigen via MHC class I, TAP-dependent	0.00394
GO:0006893	Golgi to plasma membrane transport	0.00401
GO:0005979	regulation of glycogen biosynthetic process	0.00405
GO:0010677	negative regulation of cellular carbohydrate metabolic process	0.00405
GO:0031340	positive regulation of vesicle fusion	0.00405
GO:0072329	monocarboxylic acid catabolic process	0.00413
GO:0023056	positive regulation of signaling	0.00424
GO:0051130	positive regulation of cellular component organization	0.00433
GO:0007254	JNK cascade	0.00434
GO:0030203	glycosaminoglycan metabolic process	0.00444
GO:0051592	response to calcium ion	0.00453
GO:0007188	adenylate cyclase-modulating G protein-coupled receptor signaling pathway	0.00469
GO:0032940	secretion by cell	0.00501
GO:0050730	regulation of peptidyl-tyrosine phosphorylation	0.00506
GO:0043406	positive regulation of MAP kinase activity	0.00506
GO:0090130	tissue migration	0.00513
GO:0030433	ubiquitin-dependent ERAD pathway	0.00534
GO:0008356	asymmetric cell division	0.00541
GO:0051653	spindle localization	0.00541
GO:0034620	cellular response to unfolded protein	0.00597
GO:0006977	DNA damage response, signal transduction by p53 class mediator resulting in cell cycle arrest	0.00605
GO:0050679	positive regulation of epithelial cell proliferation	0.00616
GO:0120035	regulation of plasma membrane bounded cell projection organization	0.00617
GO:0035020	regulation of Rac protein signal transduction	0.00639
GO:0006895	Golgi to endosome transport	0.00639
GO:0007608	sensory perception of smell	0.00639
GO:0006687	glycosphingolipid metabolic process	0.00639
GO:0051352	negative regulation of ligase activity	0.00642

GO:0051444	negative regulation of ubiquitin-protein transferase activity	0.00642
GO:0006904	vesicle docking involved in exocytosis	0.00679
GO:0050851	antigen receptor-mediated signaling pathway	0.00679
GO:0019933	cAMP-mediated signaling	0.00679
GO:0000916	actomyosin contractile ring contraction	0.00679
GO:0044273	sulfur compound catabolic process	0.00702
GO:0001745	compound eye morphogenesis	0.00713
GO:0007596	blood coagulation	0.00741
GO:0005975	carbohydrate metabolic process	0.0076
GO:0043062	extracellular structure organization	0.00778
GO:0061640	cytoskeleton-dependent cytokinesis	0.00794
GO:0010647	positive regulation of cell communication	0.00805
GO:0001505	regulation of neurotransmitter levels	0.00823
GO:0044262	cellular carbohydrate metabolic process	0.00833
GO:1904062	regulation of cation transmembrane transport	0.00835
GO:0045921	positive regulation of exocytosis	0.00843
GO:0002474	antigen processing and presentation of peptide antigen via MHC class I	0.00868
GO:0070207	protein homotrimerization	0.009
GO:0071377	cellular response to glucagon stimulus	0.009
GO:0019673	GDP-mannose metabolic process	0.009
GO:0075306	regulation of conidium formation	0.009
GO:0007144	female meiosis I	0.009
GO:0002673	regulation of acute inflammatory response	0.009
GO:0044091	membrane biogenesis	0.009
GO:0030866	cortical actin cytoskeleton organization	0.00906
GO:0030258	lipid modification	0.00916
GO:0006984	ER-nucleus signaling pathway	0.00921
GO:0048599	oocyte development	0.00929
GO:0048488	synaptic vesicle endocytosis	0.00931
GO:0090288	negative regulation of cellular response to growth factor stimulus	0.00951
GO:0010863	positive regulation of phospholipase C activity	0.00951
GO:0001667	ameboidal-type cell migration	0.00972
GO:0097164	ammonium ion metabolic process	0.00983
GO:0001933	negative regulation of protein phosphorylation	0.00983
GO:0046879	hormone secretion	0.00997
Cluster 7		
GO:0008045	motor neuron axon guidance	2.6e-09
GO:0033121	regulation of purine nucleotide catabolic process	3.9e-07
GO:0009118	regulation of nucleoside metabolic process	4.4e-07
GO:0072015	glomerular visceral epithelial cell development	4.2e-05
GO:0003382	epithelial cell morphogenesis	6.6e-05
GO:0007155	cell adhesion	8.4e-05
GO:0031578	mitotic spindle orientation checkpoint	1,00E-04
GO:0001736	establishment of planar polarity	0.00012
GO:0050680	negative regulation of epithelial cell proliferation	0.00012
GO:0043547	positive regulation of GTPase activity	0.00014
GO:0045571	negative regulation of imaginal disc growth	0.00019
GO:0071260	cellular response to mechanical stimulus	0.00019

GO:0042491	inner ear auditory receptor cell differentiation	2,00E-04
GO:0019991	septate junction assembly	0.00026
GO:0043588	skin development	0.00031
GO:0007160	cell-matrix adhesion	0.00037
GO:0016321	female meiosis chromosome segregation	0.00043
GO:0030334	regulation of cell migration	0.00044
GO:0007136	meiotic prophase II	0.00049
GO:0045061	thymic T cell selection	0.00049
GO:2000311	regulation of AMPA receptor activity	0.00049
GO:0033563	dorsal/ventral axon guidance	0.00055
GO:0000916	actomyosin contractile ring contraction	0.00055
GO:0030029	actin filament-based process	0.00063
GO:0019954	asexual reproduction	0.00067
GO:0042048	olfactory behavior	8,00E-04
GO:0090529	cell septum assembly	8,00E-04
GO:0002286	T cell activation involved in immune response	8,00E-04
GO:0035120	post-embryonic appendage morphogenesis	0.00087
GO:0035114	imaginal disc-derived appendage morphogenesis	0.00095
GO:2000146	negative regulation of cell motility	0.00106
GO:0043087	regulation of GTPase activity	0.00121
GO:0043542	endothelial cell migration	0.00134
GO:0061245	establishment or maintenance of bipolar cell polarity	0.00134
GO:0008104	protein localization	0.00139
GO:0070863	positive regulation of protein exit from endoplasmic reticulum	0.00144
GO:0033599	regulation of mammary gland epithelial cell proliferation	0.00144
GO:0032232	negative regulation of actin filament bundle assembly	0.00144
GO:1900006	positive regulation of dendrite development	0.00144
GO:0051764	actin crosslink formation	0.00144
GO:0000281	mitotic cytokinesis	0.00145
GO:0071478	cellular response to radiation	0.00176
GO:0003008	system process	0.00189
GO:0060070	canonical Wnt signaling pathway	0.002
GO:1905330	regulation of morphogenesis of an epithelium	0.00201
GO:0030856	regulation of epithelial cell differentiation	0.00201
GO:0048570	notochord morphogenesis	0.00201
GO:0043113	receptor clustering	0.00201
GO:0001525	angiogenesis	0.00209
GO:0006928	movement of cell or subcellular component	0.00229
GO:0001935	endothelial cell proliferation	0.00233
GO:0007391	dorsal closure	0.00233
GO:0007560	imaginal disc morphogenesis	0.00252
GO:0051493	regulation of cytoskeleton organization	0.00254
GO:0001764	neuron migration	0.00257
GO:0031100	animal organ regeneration	0.00257
GO:0006468	protein phosphorylation	0.00259
GO:2000114	regulation of establishment of cell polarity	0.00284
GO:0032489	regulation of Cdc42 protein signal transduction	0.00284
GO:0030835	negative regulation of actin filament depolymerization	0.00284

GO:0051971	positive regulation of transmission of nerve impulse	0.00284
GO:0010091	trichome branching	0.00284
GO:0003094	glomerular filtration	0.00284
GO:0048646	anatomical structure formation involved in morphogenesis	0.00307
GO:0051056	regulation of small GTPase mediated signal transduction	0.0032
GO:0046847	filopodium assembly	0.00322
GO:0035220	wing disc development	0.00349
GO:0035023	regulation of Rho protein signal transduction	0.00367
GO:0007264	small GTPase mediated signal transduction	0.00391
GO:0034333	adherens junction assembly	0.00399
GO:2000027	regulation of animal organ morphogenesis	0.00399
GO:0060562	epithelial tube morphogenesis	0.00443
GO:0030582	reproductive fruiting body development	0.00462
GO:0030708	germarium-derived female germ-line cyst encapsulation	0.00466
GO:0048846	axon extension involved in axon guidance	0.00466
GO:0045730	respiratory burst	0.00466
GO:0035204	negative regulation of lamellocyte differentiation	0.00466
GO:0008302	female germline ring canal formation, actin assembly	0.00466
GO:0050665	hydrogen peroxide biosynthetic process	0.00466
GO:0042554	superoxide anion generation	0.00466
GO:0036360	sorocarp stalk morphogenesis	0.00466
GO:1901069	guanosine-containing compound catabolic process	0.00519
GO:0008360	regulation of cell shape	0.00519
GO:0040039	inductive cell migration	0.00566
GO:0009887	animal organ morphogenesis	0.00571
GO:0007009	plasma membrane organization	0.00573
GO:0001838	embryonic epithelial tube formation	0.00573
GO:0051049	regulation of transport	0.00613
GO:0050764	regulation of phagocytosis	0.00677
GO:0051026	chiasma assembly	0.00689
GO:0000915	actomyosin contractile ring assembly	0.00689
GO:0050806	positive regulation of synaptic transmission	0.00689
GO:0032510	endosome to lysosome transport via multivesicular body sorting pathway	0.00689
GO:0046755	viral budding	0.00689
GO:0003081	regulation of systemic arterial blood pressure by renin-angiotensin	0.00689
GO:0048812	neuron projection morphogenesis	0.0069
GO:0042060	wound healing	0.00693
GO:0007265	Ras protein signal transduction	0.00709
GO:0046039	GTP metabolic process	0.00762
GO:0044766	multi-organism transport	0.00791
GO:0098609	cell-cell adhesion	0.0081
GO:0060538	skeletal muscle organ development	0.0081
GO:0010769	regulation of cell morphogenesis involved in differentiation	0.00854
GO:0021953	central nervous system neuron differentiation	0.00916
GO:0070507	regulation of microtubule cytoskeleton organization	0.00939
GO:0072089	stem cell proliferation	0.00939
GO:0051645	Golgi localization	0.00951
GO:0045887	positive regulation of synaptic growth at neuromuscular junction	0.00951

GO:0044130	negative regulation of growth of symbiont in host	0.00951
GO:0010596	negative regulation of endothelial cell migration	0.00951
GO:0051492	regulation of stress fiber assembly	0.00951
GO:0035090	maintenance of apical/basal cell polarity	0.00951
GO:0031103	axon regeneration	0.00951
GO:0048592	eye morphogenesis	0.00965
Cluster 8		
GO:0008285	negative regulation of cell population proliferation	0.00016
GO:0007169	transmembrane receptor protein tyrosine kinase signaling pathway	0.00088
GO:0007267	cell-cell signaling	0.00101
GO:0030336	negative regulation of cell migration	0.00105
GO:0034109	homotypic cell-cell adhesion	0.00183
GO:0007596	blood coagulation	0.00194
GO:0032387	negative regulation of intracellular transport	0.00259
GO:0045765	regulation of angiogenesis	0.00302
GO:0051612	negative regulation of serotonin uptake	0.00313
GO:0007263	nitric oxide mediated signal transduction	0.00313
GO:0042738	exogenous drug catabolic process	0.00313
GO:0009725	response to hormone	0.00401
GO:0051224	negative regulation of protein transport	0.0045
GO:0010959	regulation of metal ion transport	0.00594
GO:0031284	positive regulation of guanylate cyclase activity	0.00626
GO:0034332	adherens junction organization	0.00657
GO:0045216	cell-cell junction organization	0.0069
GO:0010038	response to metal ion	0.00858
GO:0006154	adenosine catabolic process	0.00937
GO:0045776	negative regulation of blood pressure	0.00937
GO:0045779	negative regulation of bone resorption	0.00937
GO:0010761	fibroblast migration	0.00937
GO:0009816	defense response to bacterium, incompatible interaction	0.00937
Cluster 9		
GO:0015991	ATP hydrolysis coupled proton transport	0.0015

Table S3.
List of genomes and transcriptomes used in the Blastn search to detect conserved S. arctica lncRNAs. SRA indicates the accession number to raw data available from the NCBI Short Read Archive. “Trinity de novo” indicates that the transcriptome was assembled without a reference genome. “Trinity de novo + ref + PASA genome” indicates that the transcriptome was assembled using a reference genome. Assembly details are described in the methods.

Species	**Transcriptome accessions (assembly strategy)**	**Genome accessions**
Sphaeroforma sirkka	SRA ERR2729814 (Trinity de novo)	
Sphaeroforma napiecek	SRA ERR2709822 (Trinity de novo)	
Sphaeroforma gastrica	Unpublished RNA-seq (Trinity de novo + ref + PASA genome)	
Sphaeroforma tapetis	Unpublished RNA-seq (Trinity de novo + ref + PASA genome)	
Sphaeroforma nootkatensis	Unpublished RNA-seq (Trinity de novo)	
Creolimax fragrantissima	SRA ERR2666850 (Trinity de novo)	
Abeoforma whisleri	Unpublished RNA-seq (Trinity de novo)	
Pirum gemmata	Unpublished RNA-seq (Trinity de novo)	
Amoebidium parasiticum	SRA SRR343044, SRR343049, SRR545192 (Trinity de novo)	
Chromosphaera perkinsii	SRA SRR5192512 (Trinity de novo)	
Ichthyophonus hoferi	SRA SRR1618711 (Trinity de novo)	
Sphaerotecum destruens	SRA SRR1618479 (Trinity de novo)	
Ministeria vibrans	SRA SRR343051, SRR343053 (Trinity de novo)	
Capsaspora owczarzaki	GCA_000151315.2	GCA_000151315.2
Salpingoeca rosetta	GCF_000188695.1	GCF_000188695.1
Monosiga brevicolis	GCF_000002865.3	GCF_000002865.3
Didymoeca costata	SRA SRR6344966 (Trinity de novo)	
Choanoeca perplexa	SRA SRR6344967 (Trinity de novo)	
Salpingoeca infusionum	SRA SRR6344968 (Trinity de novo)	
Microstomoeca roanoka	SRA SRR6344969 (Trinity de novo)	
Diaphanoeca grandis	SRA SRR6344970 (Trinity de novo)	
Acanthoeca spectabilis	SRA SRR6344971 (Trinity de novo)	
Salpingoeca dolichothecata	SRA SRR6344972 (Trinity de novo)	
Codosiga hollandica	SRA SRR6344973 (Trinity de novo)	
Salpingoeca helianthica	SRA SRR6344974 (Trinity de novo)	
Mylnosiga fluctuans	SRA SRR6344975 (Trinity de novo)	
Salpingoeca punica	SRA SRR6344976 (Trinity de novo)	
Hartaetosiga gracilis	SRA SRR6344977 (Trinity de novo)	
Salpingoeca kvevrii	SRA SRR6344978 (Trinity de novo)	
Salpingoeca urceolata	SRA SRR6344979 (Trinity de novo)	
Stephanoeca diplocostata	SRA SRR6344980 (Trinity de novo)	
Helgoeca nana	SRA SRR6344981 (Trinity de novo)	
Stephanoeca diplocostata	SRA SRR6344982 (Trinity de novo)	
Savillea parva	SRA SRR6344983 (Trinity de novo)	
Salpingoeca macrocollata	SRA SRR6344984 (Trinity de novo)	
Hartaetosiga balthica	SRA SRR6344985 (Trinity de novo)	